BRILLOUIN SCATTERING STUDIES IN SIMPLE LIQUIDS: OXYGEN AND NITROGEN

IAN ERIC MORGAN

copy 2

101187

ONE ARTICLE; IN APPENDIX A,

NOT MICROFILMED FOR REASONS OF COPYRIGHT.

M.J. Clouter, H. Kiefte, and I.E. Morgan.
Velocity of Hypersonic Waves in Liquid Oxygen,
Part II, Can. J. Phys., Vol. 53, 1975.

BRILLOUIN SCATTERING STUDIES IN SIMPLE LIQUIDS:

OXYGEN AND NITROGEN

by

© Ian Eric Morgan, B.Sc. (Hons.)

A Thesis submitted in partial fulfillment
of the requirements for the degree of
Master of Science

Department of Physics
Memorial University of Newfoundland

February 1976

St. John's Newfoundland

ABSTRACT

Thermal Brillouin scattering techniques were used to determine the velocity and attenuation of hypersonic (0.4 to 5 GHz) waves in liquid oxygen and nitrogen. Each liquid was maintained under conditions of equilibrium with its vapour, and experiments were carried out over the temperature range from the normal boiling point (T_{nbp}) to within 1 K of the critical point (T_c) in each case (90.19 K to 154.58 K for liquid oxygen, and 77.36 K to 126.26 K for liquid nitrogen).

Light from a frequency stabilized Ar^+ laser was focused at the centre of a temperature controlled cell containing the liquid sample. Light scattered at 90^0 was then analyzed by a Fabry-Perot interferometer, the transmitted light being detected by a cooled photomultiplier tube. After phase-sensitive amplification, the resulting Brillouin spectrum was displayed on a chart recorder.

The hypersonic velocity results obtained showed excellent agreement with the corresponding ultrasonic (1.2 MHz) velocities obtained from the literature for both liquids except for temperatures near the respective critical points. In this region the hypersonic velocities obtained for both liquids were lower in magnitude than the corresponding ultrasonic velocities. For oxygen (T_c = 154.58 K) this discrepancy increased from 4% at 150 K to 13% at 153.9 K, while for nitrogen (T_c = 126.26 K) this discrepancy ranged from ~ 1% at 123.7 K to ~ 3% at 125.5 K. Since these discrepancies are significantly greater than the estimated errors in these regions (a maximum of ± 1% for the hypersonic velocities, ± 0.05% for the ultrasonic velocities), it is concluded that

these saturated liquids exhibit significant negative dispersion in the sound velocities at temperatures immediately below the critical point.

Measurements of the acoustic absorption coefficient were also made in these same temperature ranges. The results obtained for both of these liquids behaved similarly. Away from the critical point (i.e., $|T - T_c| > 10$ K), the absorption coefficient was found to increase gradually with temperature such that the ratio of the absorption coefficient to the square of the hypersonic frequency varied approximately linearly with temperature. However, as the critical region was approached further ($|T - T_c| \leq 10$ K), the absorption coefficient increased rapidly by approximately one order of magnitude. Such a behaviour appears to be characteristic of these critical regions.

ACKNOWLEDGEMENTS

The author wishes to acknowledge with thanks Dr. M. J. Clouter and Dr. H. Kiefte for their continual interest and guidance throughout the course of this work and in the preparation of the thesis. Also, I wish to thank Mr. Terry White and his staff for their valuable assistance in the construction of much of the apparatus used, as well as to Messrs. Paul Stone and Roger Guest who devoted much time to the reproduction of the figures suitable for presentation. The assistance of Mr. Fred Hubley is also appreciated. Special thanks go to my wife, Sandra, and to Miss Deanna Janes who devoted much time in typing this work.

Finally, the financial assistance of the National Research Council of Canada in the form of a postgraduate scholarship is gratefully acknowledged.

TABLE OF CONTENTS

LIST OF TABLES

LIST OF FIGURES

Page

CHAPTER 1

INTRODUCTION

1.1 Historical Introduction

Brillouin scattering is the inelastic scattering of light from propagating thermally generated density fluctuations or sound waves in a medium. This type of scattering was initially proposed by Léon Brillouin in 1914 and later published with completeness in 1922. He predicted that the frequency spectrum of the light scattered in a homogeneous medium should contain a fine structure consisting of a doublet, symmetrically positioned about the frequency of the incident light. This doublet, with characteristic frequency shifts of a few GHz, was first observed experimentally by Gross in 1930 and 1932 in liquids.

Between 1930 and 1960 the Brillouin spectra were observed for a variety of substances by a number of investigators, particularly by Venkateswaren (1942) in liquids and Krishnan (1955) in solids. The light sources most commonly used in these early experiments were low pressure arc lamps, usually the Hg lamp, where the isotope effect and hyperfine structure limited the degree of monochromaticity attainable. An approximately monochromatic and parallel beam was obtained using filters and standard collimation techniques, usually resulting in low workable intensities. Thus the lack of monochromaticity and the relatively low intensity of these light sources placed strong limitations on the observation of this phenomenon; that is, the broad natural width of the source spectrum made it difficult to resolve the Brillouin doublet and

almost impossible to determine their natural line widths. Consequently, one finds considerable discrepancies in the limited velocity results obtained by these earlier investigators.

With the advent in the early 1960's of the laser as an intense monochromatic light source, and also with the development of high resolution Fabry-Perot interferometry, these difficulties were effectively overcome and this field of Brillouin scattering received considerable attention. Chiao and Stoicheff (1964) and Benedek et al. (1964) were among the first to observe the Brillouin effect in liquids using a He-Ne laser and Fabry-Perot interferometry. In subsequent years many investigators have obtained reliable values of hypersonic velocity with accuracies better than ± 0.1% although the accuracy in the measurement of the Brillouin line widths is somewhat less, due to the difficulties in separating the natural line width from the instrumental broadening (Leidecker and LaMacchia (1968)).

1.2 Brillouin Effect

The frequency shifts of the incident light in Brillouin scattering can be derived simply by considering the interaction between a light wave of frequency ν_i and wavelength λ_i and a hypersonic or ultrasonic plane wave travelling in a given medium with frequency ν_s and velocity $\vec{V}$. Such sound waves can be represented as plane parallel regions of higher or lower densities and, if the waves were stationary, one would expect to have the optical analog of Bragg scattering of X-rays by lattice planes in a crystal as shown in Figure 1.1.

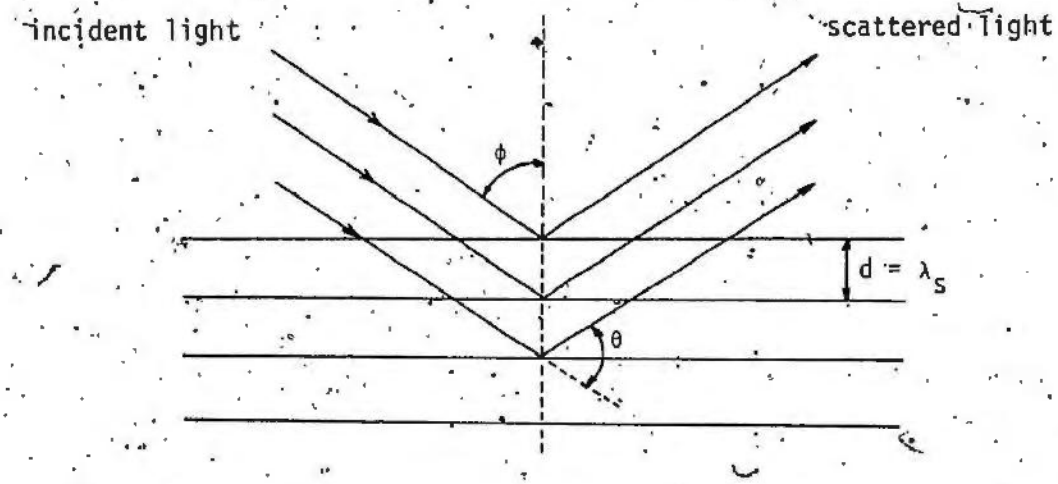

FIGURE 1.1

The result is selective scattering (constructive interference) of light by the sound wave in accordance with the Bragg (coherence) condition, that is when

$$m\lambda_i = 2nd \cos \phi \qquad (1.1)$$

where m is the order of scattering number;

n is the index of refraction of the medium at the wavelength λ_i;

$d = \lambda_s$ is the distance between successive wavefronts;

and ϕ is the angle of incidence.

Since the angle of incidence must equal the angle of reflection, the scattering angle θ becomes $\theta = \pi - 2\phi$. Because scattering processes for which $m > 1$ are not observed in practice, we restrict ourselves to

considering only first-order scattering (m=1). Equation (1.1) then becomes:

$$\lambda_i = 2nd \sin\left(\frac{\theta}{2}\right) = 2n\lambda_s \sin\left(\frac{\theta}{2}\right) . \qquad (1.2)$$

If the sound wave of Figure 1.1 were propagating with a velocity $\vec{V}$ whose magnitude is given by $V = \lambda_s \nu_s$, then the light reflected from the sound wave would undergo a Doppler shift of magnitude:

$$\Delta\nu_i \equiv \pm \nu_s = \pm \frac{2nV}{c} \nu_i \sin\left(\frac{\theta}{2}\right) . \qquad (1.3)$$

where c is the velocity of light in <u>vacuo</u> and the plus and minus signs are inserted to account for the shift in frequency of light scattered from a sound wave approaching or receding from the light source. Equation (1.3), first deduced by Brillouin, is known as the Brillouin Equation.

The connection between the simple example and the real case is provided by the method of Fourier synthesis: the thermally generated density fluctuations in a real medium can be represented by an appropriate Fourier superposition of sinusoidal and monochromatic plane waves. It is then, in effect, these individual Fourier components which are observable by Brillouin scattering since the choice of a particular scattering angle (θ) and incident optical wavelength (λ_i) automatically determines (via equation (1.2)) both the directions and wavelength of the density fluctuations to be detected.

The Brillouin Equation can also be obtained quantum mechanically by considering the effect as an interaction between an incident photon and

a phonon beam or sound wave in the medium resulting in the creation (or annihilation) of a photon as depicted in Figure 1.2(a).

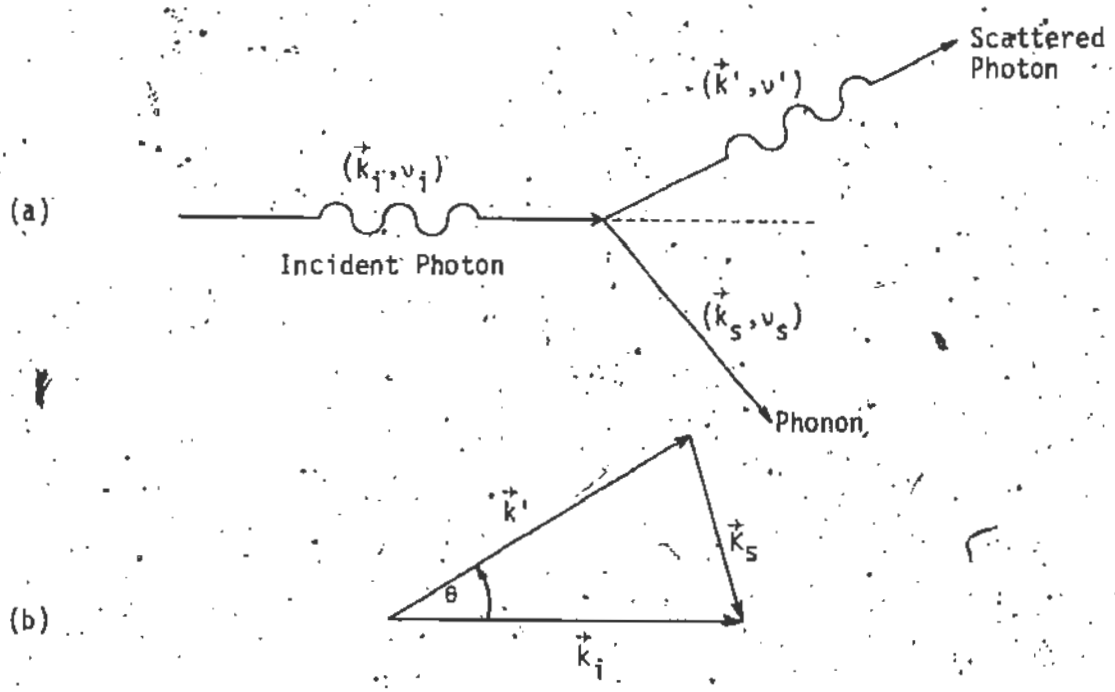

FIGURE 1.2

By conservation of energy and momentum,

$$h\nu_i - h\nu' = \pm h\nu_s \qquad (1.4)$$

$$\hbar\vec{k}_i - \hbar\vec{k}' = \pm \hbar\vec{K}_s \quad , \qquad (1.5)$$

with $\hbar = h/2\pi$, where h is Planck's constant, and the plus and minus signs have the same significance as in equation (1.3) and correspond to the Stokes and anti-Stokes scattering, respectively. The wave vectors $(\vec{k})$ are related to the frequencies (ν) and the indices of refraction (n) by:

$$2\pi\nu_i = \omega_i = \frac{k_i c}{n_i} \; ; \quad 2\pi\nu' = \omega' = \frac{k' c}{n'} \; ; \quad 2\pi\nu_s = \omega_s = k_s V \qquad (1.6)$$

where $\frac{c}{n_i} \simeq \frac{c}{n'} \cong \frac{c}{n}$ and V are the speed of light and sound in the medium, respectively. The first equation (1.4) identifies the sound frequency, ω_s, as that of the frequency shift of the scattered light, while the second equation (1.5) gives the vector relation shown in Figure 1.2(b).

Since the speed of sound, V, is much less than the speed of light, c, it follows that $\omega_i >> \omega_s$ and thus $\nu_i \simeq \nu'$ and $\vec{k}_i \simeq \vec{k}'$. If $\vec{k}_i \simeq \vec{k}'$, then from Figure 2.1(b) we get:

$$k_s \cong 2k_i \, \mathrm{Sin}\left(\frac{\theta}{2}\right) . \qquad (1.7)$$

Upon substituting the relations $\omega_s = Vk_s$ and $\omega_i = \frac{k_i c}{n}$ in equation (1.7), we again obtain the Brillouin Equation, thus:

$$\nu_s = \frac{2V\nu_i n}{c} \, \mathrm{Sin}\left(\frac{\theta}{2}\right) . \qquad (1.8)$$

Thus, by measuring the frequency shifts (ν_s) of the two Brillouin components, the hypersonic velocities at these frequencies, as well as their angular dependence, can be determined from the Brillouin Equation. However, it is well known that sound waves traversing a medium suffer appreciable attenuation and hence have a finite lifetime; this effect is reflected in each member of the Brillouin doublet which also has a finite width. Since the Brillouin Equation does not give the spectral distribution of the scattered light, a more complete theory is necessary to predict this broadening effect.

1.3 Classical Theory of Brillouin Scattering in Liquids

Since the experiments to be described in this thesis involve Brillouin scattering in liquids only, we now restrict our discussions accordingly. The appropriate classical theory has been presented by Benedek and Greytak (1965) as well as Gornall (1966), and will be reviewed below.

Let an incident wave,

$$\vec{E}_{inc}(\vec{r},t) = \vec{E}_{oi} \exp(i(\vec{k}_i \cdot \vec{r} - \omega_i t)) \qquad (1.9)$$

impinge on a medium (see Figure 1.3). This wave polarizes the medium producing an oscillating polarization $\vec{P}(\vec{r},t)$ at each point $\vec{r}$ in the medium. This oscillating polarization in the volume element $|d\vec{r}|$ of the illuminated volume radiates an electric field whose strength at the field point, $\vec{R}$, is given by:

$$d\vec{E}_{scat}(\vec{R},t) = \frac{\ddot{\vec{P}}(\vec{r},t - |\vec{R}-\vec{r}|/c) \sin\phi \; |d\vec{r}|}{c^2 |\vec{R}-\vec{r}|} \qquad (1.10)$$

where ϕ is the angle between the incident $\vec{E}$ field and the wave vector, $\vec{k}'$, of the scattered light, and $\ddot{\vec{P}}$ is the second-order time derivative of the polarization, $\vec{P}$.

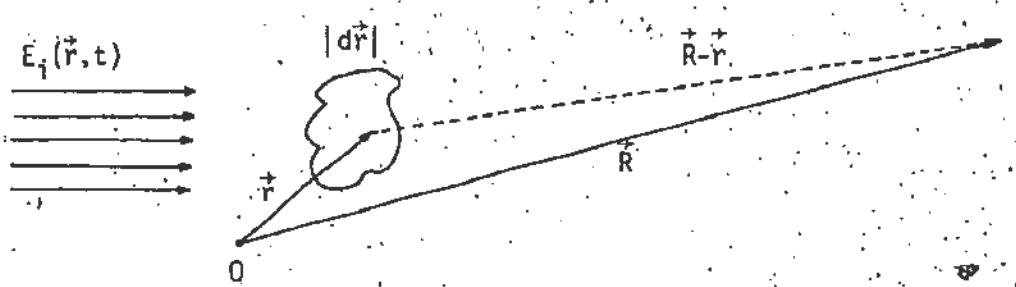

FIGURE 1.3

The polarization, $\vec{P}(\vec{r},t)$, is related to the incident field, $\vec{E}_{inc}(\vec{r},t)$, via the electric polarizability, $\alpha(\vec{r},t)$, of the medium; i.e.,

$$\vec{P}(\vec{r},t) = \alpha(\vec{r},t)\vec{E}_{inc}(\vec{r},t) \quad , \tag{1.11}$$

where $\alpha(\vec{r},t)$ is related to the dielectric constant, ε, by:

$$\alpha(\vec{r},t) = [(\varepsilon(\vec{r},t) - 1)/4\pi] \quad . \tag{1.12}$$

Taking $\vec{R} >> \vec{r}$ and neglecting the small change in wavelength of the scattered light, the electric field scattered at $\vec{R}$ by the total illuminated volume, v, becomes:

$$\vec{E}_{scat}(\vec{R},t) \simeq \vec{E}_{oi}(\omega_o/c)^2 \frac{\exp(i(\vec{k}'\cdot\vec{R} - \omega_i t))\ \text{Sin}\ \phi}{\vec{R}} \int_v \alpha(\vec{r},t)\ e^{i(\vec{k}-\vec{k}')\cdot\vec{r}}\ |d\vec{r}| \tag{1.13}$$

where $\vec{k}' = \frac{(2\pi n)}{\lambda_i}\hat{e}'$ is the scattered wave vector and $\hat{e}'$ is a unit vector in the direction of the scattered beam. Therefore, the scattered field is a spherically spreading wave whose amplitude is determined by the interference integral:

$$I = \int_v \alpha(\vec{r},t)\ e^{-\vec{K}\cdot\vec{r}}\ |d\vec{r}| \tag{1.14}$$

where $\vec{K} = \vec{k}'-\vec{k}$. This interference integral represents the superposition of phases of waves scattered from each point in the illuminated volume.

If we write the polarizability in terms of its average value and the fluctuations about the average, i.e.,

$$\alpha(\vec{r},t) = \langle\alpha\rangle + \delta\alpha(\vec{r},t) \quad , \tag{1.15}$$

upon substituting (1.14) into (1.13) we find that the time independent (average) polarizability $\langle\alpha\rangle$ produces scattering only in the forward direction, i.e., $\vec{K} = 0$, and therefore any scattering in directions other than the forward direction arises entirely from the fluctuation term, $\delta\alpha(\vec{r},t)$, in the polarizability. To find the fluctuation causing the scattering in the direction, $\vec{k}'$, we write the fluctuations in α in terms of its Fourier components; i.e.,

$$\delta\alpha(\vec{r},t) = \frac{1}{(2\pi)^{3/2}} \int |d\vec{q}|\ \exp(i\vec{q}\cdot\vec{r})\ \delta\alpha(\vec{q},t) \qquad (1.16)$$

Substituting into equation (1.14) we get:

$$I = \frac{1}{(2\pi)^{3/2}} \int |d\vec{q}|\ \delta\alpha(\vec{q},t) \int_V \exp(i(\vec{q}-\vec{K})\cdot\vec{r})\ |d\vec{r}|. \qquad (1.17)$$

where

$$\int_V \exp(i(\vec{q}-\vec{K})\cdot\vec{r})\ |d\vec{r}| = (2\pi)^3\delta(\vec{q}-\vec{K}) \qquad (1.18)$$

where $\delta(\vec{q}-\vec{K})$ is the Dirac delta function.

This result is equivalent to the Bragg reflection condition discussed previously, since it shows that the scattering in the direction $\vec{k}'$ is produced by a fluctuation whose wave vector $\vec{q}$ equals the scattering vector $\vec{K}$.

Using $\delta\alpha(\vec{r},t) = \frac{\delta\epsilon(\vec{r},t)}{4\pi}$ and substituting (1.18) and (1.17) into (1.13), we get:

$$\vec{E}_{scat}(\vec{R},t) = \frac{\vec{E}_o\left(\frac{\omega_i}{c}\right)^2 e^{i(\vec{k}\cdot\vec{R} - \omega_i t)}\ \text{Sin}\ \phi}{4\pi\vec{R}} (2\pi)^{3/2}\ \delta\epsilon(\vec{K},t) \qquad (1.19)$$

where $\delta\epsilon(\vec{K},t) = \frac{1}{(2\pi)^{3/2}} \int |d\vec{r}| \exp(-i\vec{K}\cdot\vec{r})\, \delta\epsilon(\vec{r},t)$ is the Fourier transform of $\delta\epsilon(\vec{r},t)$ given as the inverse of equation (1.16).

To determine the frequency spectrum of the scattered light intensity, we make use of the fact that the spectrum density of $\vec{E}^2_{scat}(\vec{R},t)$ is the Fourier transform of the correlation function of the scattered field. The correlation function is defined as $R_E(\tau)$, where τ is defined as the correlation time, such that:

$$R_E(\tau) = \langle \vec{E}_{scat}(\vec{R},t+\tau)\cdot\vec{E}^*_{scat}(\vec{R},t)\rangle$$

$$= \lim_{T\to\infty} \frac{1}{2T} \int_{-T}^{T} \vec{E}_{scat}(\vec{R},t+\tau)\cdot\vec{E}^*_{scat}(\vec{R},t)dt \qquad (1.20)$$

with the property that $R_E(\tau) = 0$ when $\tau<0$.

The spectral density is then given as:

$$S(\vec{K},\omega) = \frac{1}{2\pi}\int_{-\infty}^{\infty} R_E(\tau)\, e^{i\omega\tau}\, d\tau \qquad (1.21)$$

using the normalization

$$\langle|\vec{E}(\vec{R},t)|^2\rangle = R_E(0) = \int_{-\infty}^{\infty} S(\vec{K},\omega)d\omega \qquad (1.22)$$

Using equation (1.19), the correlation function $R_E(\tau)$ can be expressed in terms of the correlation in $\delta\epsilon(\vec{K},t)$, i.e.,

$$R_E(\tau) = E^2_{oi}(\omega_i/c)^4 \frac{\sin^2\phi}{(4\pi R)^2} (2\pi)^3 e^{-i\omega_i\tau} R_{\delta\epsilon}(\tau) \qquad (1.23)$$

The spectral density then becomes:

$$S(\vec{k},\omega) = \vec{E}_{oi}^2 \left(\frac{\omega_i}{c}\right)^4 \frac{\sin^2\phi}{(4\pi R)^2} (2\pi)^3 \cdot \frac{1}{2\pi} \int_{-\infty}^{\infty} R_{\delta\varepsilon}(\tau)\, e^{i\omega_i \tau}\, e^{i\omega\tau}\, d\tau \,. \quad (1.24)$$

The problem now reduces to finding an expression for $R_{\delta\varepsilon}(\tau)$, where

$$R_{\delta\varepsilon}(\tau) = \langle \delta\varepsilon(\vec{K},t+\tau)\delta\varepsilon^*(\vec{K},t)\rangle \,. \quad (1.25)$$

To accomplish this, we consider $\delta\varepsilon$ as a function of two independent thermodynamic variables, pressure and entropy; we have

$$\delta\varepsilon = \left(\frac{\partial\varepsilon}{\partial p}\right)_S \delta p + \left(\frac{\partial\varepsilon}{\partial S}\right)_p \delta S \quad (1.26)$$

and, assuming the fluctuations in p and S are uncorrelated, we may consider each term separately. The first term corresponds to adiabatic pressure fluctuations which constitute sound waves, thus:

$$\{\delta\varepsilon(\vec{K},t)\}_S = \left(\frac{\partial\varepsilon}{\partial p}\right)_S \{\delta p(\vec{K},t)\}_S \,. \quad (1.27)$$

Here, $\delta p(\vec{K},t)$ is the Fourier amplitude of the spatial component of pressure, having the wavelength $2\pi/K$. Assuming the sound wave, i.e., pressure fluctuations, travels with angular frequency $\pm\omega_s(\vec{K})$ and has a lifetime $1/\Gamma(\vec{K})$, the correlation function for the pressure fluctuations becomes:

$$R_{\delta p}(\tau) = \langle \delta p(\vec{K},t+\tau)\delta p^*(\vec{K},t)\rangle = \langle |\delta p(\vec{K},t)|^2\rangle\, e^{\pm i\omega_s\tau}\, e^{-\Gamma|\tau|} \,. \quad (1.28)$$

Thus:

$$\left[R_{\delta\varepsilon}(\tau)\right]_{\substack{\text{sound}\\\text{wave}}} = \left(\frac{\partial\varepsilon}{\partial p}\right)_S^2 \langle|\delta p(\vec{K},t)|^2\rangle\, e^{\pm i\omega_s\tau}\, e^{-\Gamma|\tau|} \quad . \tag{1.29}$$

Substituting (1.29) into (1.24) we get:

$$\left[S(K,\omega_s)\right]_{\substack{\text{sound}\\\text{wave}}} = E_{oi}^2 \left(\frac{\omega_i}{c}\right)^4 \frac{\sin^2\phi}{(4\pi R)^2}(2\pi)^3 \left(\frac{\partial\varepsilon}{\partial p}\right)_S^2 \langle|\delta p(\vec{K},t)|^2\rangle \frac{1}{\pi} \cdot$$

$$\frac{\Gamma(\vec{K})}{\Gamma(\vec{K})^2 + (\omega-(\omega_i-\omega_s(\vec{K})))^2} + \frac{\Gamma(\vec{K})}{\Gamma(\vec{K})^2 + (\omega-(\omega_i+\omega_s(\vec{K})))^2} \quad . \tag{1.30}$$

These last two terms represent the two Brillouin lines, centered at the frequencies $\omega = \omega_i-\omega_s$ and $\omega = \omega_i+\omega_s$, broadened by an amount determined by the 'lifetime' $1/\Gamma$ of the frequency ω_s: this line shape is commonly called Lorentzian with full width at half intensity given by;

$$\Delta\nu(\vec{K}) = \frac{\Gamma(\vec{K})}{\pi} \quad . \tag{1.31}$$

Thus, from the measurements of $\omega_s = \omega-\omega_i$ and the line width $\Delta\nu(\vec{K})$, one can determine not only the speed of sound at the frequency ω_s but also the decay rate of the sound waves in the medium. The amplitude absorption coefficient is then defined as:

$$\alpha(\vec{K}) = \frac{\pi\Delta\nu(\vec{K})}{V(\vec{K})} \tag{1.32}$$

where $V(\vec{K})$ is the speed of sound at the frequency ω_s.

1.4 Propagation of Acoustic Waves in Liquids

The preceding discussion indicates how the velocity and attenuation of sound waves in a given liquid can be determined from Brillouin scattering studies. From a consideration of hydrodynamic theory we now show how this information can be related to the characteristic bulk properties of the liquid.

If one first considers a longitudinal wave propagating in an isotropic homogeneous medium, then the particles of the medium move in an oscillatory manner in the direction of wave propagation. We consider the motion of an element of the medium which is small in comparison with the sound wavelength and which is initially contained between two parallel plates, A and B, of unit area (Figure 1.4). These plates are at right

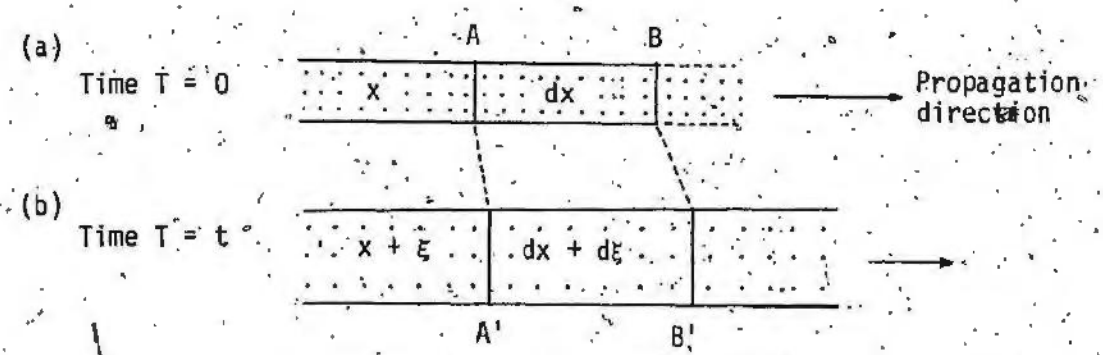

FIGURE 1.4

angles to the propagation direction and (in the one-dimensional case) are at distances x and x + dx from some reference point. If ρ is the initial density of the medium in the absence of the sound wave, the mass of the element is ρdx. After a time t the element is displaced to a new position A'B' where A' is a distance $(x + \xi)$ from the origin and the

length of the element is now $(dx + d\xi)$. From conservation of mass considerations, the new value of density becomes

$$\rho' = \rho \frac{dx}{dx + d\xi} = \rho\left(1 - \frac{\partial \xi}{\partial x}\right) \tag{1.33}$$

for small displacements. The net force acting on the displaced element is $(p_{A'} - p_{B'})$, where p is the hydrostatic pressure. Equating this force to the product of the mass of the fluid contained in the volume element and its acceleration (Newton's equation), we get:

$$p_{A'} - p_{B'} = -\frac{\partial p}{\partial x} dx = \rho dx \frac{d^2\xi}{dt^2} \tag{1.34}$$

Thus:

$$\rho \frac{d^2\xi}{dt^2} = -\frac{\partial p}{\partial x} = -\frac{\partial p}{\partial \rho} \cdot \frac{\partial \rho}{\partial x} = \rho \frac{\partial p}{\partial \rho} \frac{d^2\xi}{dx^2} \tag{1.35}$$

and the equation of motion of the element becomes:

$$\frac{d^2\xi}{dt^2} = \frac{\partial p}{\partial \rho} \frac{d^2\xi}{dx^2} \tag{1.36}$$

which is the equation of wave motion where $\left(\frac{\partial p}{\partial \rho}\right)$ has the dimensions of a square of a velocity $\vec{V}$:

$$V^2 = \frac{\partial p}{\partial \rho} \tag{1.37}$$

The solution of equation (1.36) for the usual case in which the particle displacement, velocity and pressure vary sinusoidally with time is:

$$\xi(x,t) = \xi_0 \exp[i\omega(t - x/\vec{V})] \tag{1.38}$$

where ξ_0 is the amplitude of the sound wave, ω is the angular frequency and $\vec{V}$ is the phase velocity. This result is valid only in the acoustic approximation which assumes that the sound waves are of such small amplitude that $\frac{\partial \xi}{\partial x} << 1$ in equation (1.33), i.e., the fluctuations in pressure δp and density $\delta \rho$ caused by the sound wave are, to first order in accuracy, negligible compared to the equilibrium values of pressure and density in the absence of the wave. If we further assume that the processes in a sound wave are adiabatic and reversible, then we may relate the sound velocity to convenient parameters of the fluid, i.e., its adiabatic bulk-modulus. The adiabatic bulk-modulus is defined as:

$$B_a = -\frac{1}{v}\left(\frac{\partial p}{\partial v}\right)_S = \rho\left(\frac{\partial p}{\partial \rho}\right)_S \qquad (1.39)$$

and equation (1.36) becomes:

$$V^2 = \frac{\partial p}{\partial \rho} = \frac{B_a}{\rho} \qquad (1.40)$$

or, equivalently,

$$V = \sqrt{B_a/\rho} \qquad (1.41)$$

Since the bulk-modulus and the density are both temperature dependent, this also suggests a temperature dependence of the sound velocity. Thus, equation (1.41) is the general result for low-amplitude, sound propagation in an idealized (non-viscous, non-absorbing) medium.

However, it is well known that acoustic waves are attenuated in passing through a real medium. The problem for the absorbing medium differs from the idealized case just considered in that one must use the Stokes equation for the propagation of sound in a viscous medium. Thus,

equation (1.36) must include an additional damping term to account for the energy loss mechanisms. In general the wave equation takes the form:

$$\ddot{\phi} - V^2\nabla^2\phi - \chi\nabla^2\dot{\phi} = 0 \qquad (1.42)$$

where ϕ is the propagating parameter of the wave, χ is the damping coefficient, and $\dot{\phi} = \frac{d\phi}{dt}$ is the time derivative of the oscillating parameter of the wave. For a medium with a finite viscosity, frictional losses occur and the wave equation becomes (in the acoustic approximation)

$$\frac{d^2\xi}{dt^2} - V^2\frac{d^2\xi}{dx^2} - \frac{1}{\rho}\left(\frac{4}{3}\eta_S + \eta_B\right)\frac{d^2\dot{\xi}}{dx^2} = 0 \qquad (1.43)$$

where $\frac{1}{\rho}\left(\frac{4}{3}\eta_S + \eta_B\right)\frac{d^2\dot{\xi}}{dx^2}$ is the required damping term, η_S is the coefficient of sheer viscosity (corresponding to the viscous drag experienced when layers of fluid move over each other), and η_B is known as the bulk viscosity. It was assumed by Stokes that η_B was identically zero and, to a large extent, this assumption marks the difference between classical and modern theories of acoustic absorption and dispersion.

Thus, placing $\eta_B = 0$ in equation (1.43), we get:

$$\frac{d^2\xi}{dt^2} = V^2\frac{d^2\xi}{dx^2} + \frac{4}{3}\frac{\eta_S}{\rho}\frac{d^3\xi}{dx^2dt} \qquad (1.44)$$

The solution of equation (1.44) is of the form:

$$\xi(x,t) = \xi_o\, e^{-\alpha x}\exp[i\omega(t - x/V)]$$

$$= \xi_o \exp\left[i\omega\left\{t - x\left(1/V - \frac{i\alpha}{\omega}\right)\right\}\right] \qquad (1.45)$$

where ξ_0 is the amplitude of the sound wave of angular frequency ω and velocity $\vec{V}$ and α is a spatial absorption coefficient of the sound wave defined such that the amplitude of the wave is attenuated by a factor of $e^{-\alpha x}$ as it propagates a distance x in the liquid. α defined in this way is the absorption coefficient which is measured in ultrasonic experiments where the decreases in amplitude of a mechanically generated sound wave is measured over a distance separating the transmitter and receiver. On the other hand, in Brillouin scattering studies, one measures a temporal absorption coefficient, α_t, because the width of the Brillouin components gives information about the decay of the temporal correlations in the sound wave. These two types of amplitude absorption coefficients are thus related by the relation:

$$\alpha = \frac{\alpha_t}{V} \qquad (1.46)$$

where $\vec{V}$ is the sound velocity in the medium which is the same as $\vec{V}_0$ (low frequency velocity limit) if α is sufficiently small. The value of the spatial absorption coefficient α_{sh} due to the shear viscosity effect may be obtained by inserting (1.45) (with $\alpha = \alpha_{sh}$) into (1.44) to give:

$$\alpha_{sh} = \frac{8}{3}\frac{\pi^2 \eta_s}{\rho V^3}\nu^2 \qquad (1.47)$$

where $\nu = \frac{\omega}{2\pi}$ is the frequency of the wave.

Thermal conductivity of the medium also leads to absorption of the acoustic waves. At any instant the high pressure regions will have a temperature above the average, while the opposite is true for the low pressure regions. Heat will be conducted from the high to the low temperature regions, and a compressed region will return less work on

expansion that was required to compress it. This leads to sound absorption, α_{th}, and it can be shown (Herzfeld and Litovitz (1959)) that:

$$\alpha_{th} = \frac{2\pi^2 \kappa(\gamma-1)\nu^2}{\rho\gamma C_v V^3} \qquad (1.48)$$

where κ is the thermal conductivity, γ is the ratio of the specific heat at constant pressure C_p and volume C_v.

The losses caused by both viscosity and thermal conductivity (those caused by the latter are usually negligible compared to the former losses), assumed additive, are combined in the classical absorption α_{cl}:

$$\alpha_{cl} = \alpha_{sh} + \alpha_{th} = \frac{2\pi^2}{\rho V^3}\left(\frac{4}{3}\eta_S + \frac{(\gamma-1)}{\gamma}\frac{\kappa}{C_v}\right)\nu^2 \qquad (1.49)$$

Hence, the classical absorption of acoustic waves in a liquid is proportional to the square of the sound frequency. However, it was found that the experimentally measured values of the absorption coefficient, α_{obs}, is always larger than the classical result, α_{cl}. This discrepancy between the experimentally observed absorption and the classically predicted result, α_{cl}, is normally attributed to a non-zero bulk viscosity, η_B (i.e., the assumption of $\eta_B = 0$ in equation (1.44) is invalid).

1.5 Relaxational Theory of Sound Absorption

This bulk viscosity in liquids is theorized to arise from two sources. The first is the energy loss associated with the flow of liquid molecules between high and low density regions during a change in volume of a given mass of the liquid, which is usually defined as a volume viscosity. The other contribution to the bulk viscosity arises from

relaxational processes involving the internal degrees of freedom of the molecules.

Relaxational theory predicts that the passage of sound upsets the thermodynamic equilibrium of the liquid such that the propagating wave couples energy into the various internal (rotational and vibrational) degrees of freedom of the system. When a time-lag exists in this transfer, that is, when the energy returned to the sound wave is out of phase, the wave suffers velocity dispersion and absorption.

In the theory, based on a single relaxation time, the energy transfer process occurs exponentially in time, characterized by a time constant τ and a corresponding relaxational frequency $\nu_r = (2\pi\tau)^{-1}$. Such a treatment gives the excess absorption α_r' due to the relaxational process as (Matheson (1970)):

$$\alpha_r' = \frac{2\pi^2\nu^2}{\rho V^3}\,\eta_B(\nu) \qquad (1.50)$$

where $\eta_B(\nu)$ is the frequency dependent bulk-viscosity.

Theory predicts various types of relaxational processes in liquids (Fabelinskii (1968), Bhatia (1967)). The most common types in the so-called normal liquids (liquids having relatively weak intramolecular forces, e.g., nitrogen and oxygen being so classified) are expected to be thermal relaxational processes, particularly vibrational relaxation where energy is coupled into the internal vibrational modes of the molecules. In the associated liquids (characterized by relatively strong intramolecular forces and high viscosity), other relaxational effects called structural relaxation can also occur. However, for the

purpose of this report, we are interested in normal liquids and, hence, only vibrational relaxation is considered.

For normal liquids, whose excess absorption may be attributed to a single thermal relaxation processes, the velocity dispersion and absorption is given by this treatment (Sette (1968)) as:

$$\left(\frac{V}{V_o}\right)^2 \simeq \frac{1 + \omega^2\tau^2}{1 + \omega^2\tau^2(1-A)} \qquad (1.51)$$

$$\alpha_r' = \frac{1V}{2V_o^2} \frac{A\omega^2\tau}{1 + \omega^2\tau^2} \qquad (1.52)$$

where

$$A = \frac{V_\infty^2 - V_o^2}{V_\infty^2} \qquad (1.53)$$

where $\vec{V}_\infty$ and $\vec{V}_o$ and the high and low frequency limits of the sound velocity, and τ is the relaxation time of the process.

Thus, from equation (1.52), we see that at very high frequencies ($\omega^2 >> \tau^{-2}$), α_r' becomes independent of ω, while at lower frequencies ($\omega^2 << \tau^{-2}$) the absorption coefficient is proportional to the square of the frequency as in the classical case:

$$\frac{\alpha_r'}{\nu^2} = \frac{2\pi^2}{V_o} A\tau \qquad (1.54)$$

For the case of normal liquids, especially those which exhibit small velocity dispersion, i.e., $\vec{V} \simeq \vec{V}_o$, the excess absorption α_r' is usually written as:

$$\frac{\alpha_r'}{\nu^2} = \frac{A_1}{1 + \omega^2\tau^2} \qquad (1.55)$$

where A_1 is considered a constant in this approximation. This absorption α_r' is normally considered additive with the classical result α_{cl} (equation (1.13)) such that the observed absorption is usually written as:

$$\alpha = \alpha_{cl} + \alpha_r' \qquad (1.56)$$

Thus, from experimentally determined values of α, equation (1:20) could allow a determination of the portion α_r' which arises due to the relaxation process occurring in the observed frequency region.

1.6 Critical Absorption

Although the previously mentioned considerations of sound absorption in liquids (based on simple hydrodynamics) are known to be quite valid for a wide temperature range, these predictions do not strictly hold for temperatures quite near the critical point. A dominant characteristic of all critical systems is the large increase of the microscopic fluctuations which can consequently reach effectively macroscopic magnitudes. The liquid can then be thought of as being composed of a distribution of molecular 'clusters' of different densities and sizes dispersed in the medium. This region is also characterized by a number of critical phenomena including the well-known critical opalescence as well as the anomalous behaviour of many, if not all, of the transport properties of the liquid which occur in the absorption coefficient equation (1.56). Experiments show (Chynoweth and Schneider (1952); Chase et al. (1964); D'Arrigo and Sette (1967); Mueller et al.

(1972)) that the absorption coefficient diverges substantially for all systems studied as the temperature approaches the critical point, T_c: the marked increase often begins at temperatures which differ from T_c by only 2-3 K. Light scattering investigations of a simple fluid near its critical point are particularly useful in providing information about the thermodynamic and dynamical behaviour concerning critical relaxation processes (Ford et al. (1968); Mohr et al. (1971); Cannell and Benedek (1970); Eden et al. (1972)).

Various theories and models have been proposed to explain the sound absorption anomaly in terms of the long-range (critical) fluctuations and the manner in which they affect the behaviour of the transport coefficients near T_c. One of the theories which seems to be reasonably successful in predicting this anomalous behaviour is based on the Scaling-law ideas (Stanley (1971)) which assumes that the divergence in the transport coefficient is proportional to some simple power law of the form $\varepsilon^{-\beta}$ where $\varepsilon = \frac{T - T_c}{T_c}$ and β is the critical point exponent which, although it is usually of the order of unity, varies from system to system. However, present theory appears to be in a state of dispute with no one theory of model predicting a general result valid for all systems over the complete critical region. Consequently, one finds that the particular theory of combination of theories applicable to a particular system is often determined from the experimental results obtained.

1.7 Thesis Outline

Although there have been extensive investigations of many room-temperature liquids and liquid mixtures performed, very few Brillouin

scattering studies of cryogenic liquids have been reported. Quite a few ultrasonic experiments have been performed on these low temperature liquids but because of technical limitations this method is usually restricted to a maximum frequency of ≈ 0.1 GHz. On the other hand, Brillouin scattering permits the study of sound propagation at (hypersonic) frequencies up to ~ 10 GHz where many liquids are expected to exhibit velocity dispersion (Fabelinskii (1968)) with a corresponding change in the absorption of the sound waves. If such a velocity dispersion were found to exist, it could provide information on relaxational phenomena in the liquids. The objective of this research was to measure the hypersonic velocity and absorption for two of these cryogenic liquids (nitrogen and oxygen) over their entire normal liquid temperature range and look for thermal relaxational effects, especially near the critical points where these effects are expected to be most pronounced.

In Chapter II, a description of the experimental apparatus used to study Brillouin scattering in liquids is given along with the procedures for hypersonic velocity and absorption measurements.

Chapter III deals with the experimental results obtained and the analysis of these results. The spectral characteristics of the scattered light as well as the measurement of the velocity and absorption for both liquids are presented for a range of temperatures up to the respective critical points. (Hypersonic velocities for O_2 below its normal boiling point, T_{nbp}, are given in the appendix for completeness.)

Chapter IV consists of a discussion of the results.

CHAPTER 2

APPARATUS AND EXPERIMENTAL TECHNIQUE

The spectroscopic techniques used in this research are now fairly common in Brillouin scattering studies (see Figure 2.1). Briefly, light from a frequency stabilized Ar+ laser was focused at the centre of a temperature controlled cell containing the liquid sample. Light scattered at 90^{0} was then analyzed by a Fabry-Perot interferometer, the transmitted light being detected by a cooled photomultiplier tube. After phase-sensitive amplification, the resulting Brillouin spectrum was displayed on a chart recorder.

The experimental apparatus and methods will be described more fully under the following headings:

1. Laser
2. Interferometer
3. Photomultiplier Tube and Detection System
4. Cell and Gas Handling System
5. Cryostat
6. Analysis Procedures

2.1 Laser

Since Brillouin spectroscopy depends on a high resolution, it requires the incident beam to be highly monochromatic and reasonably intense.

FIGURE 2.1

Block diagram of the overall experimental apparatus.

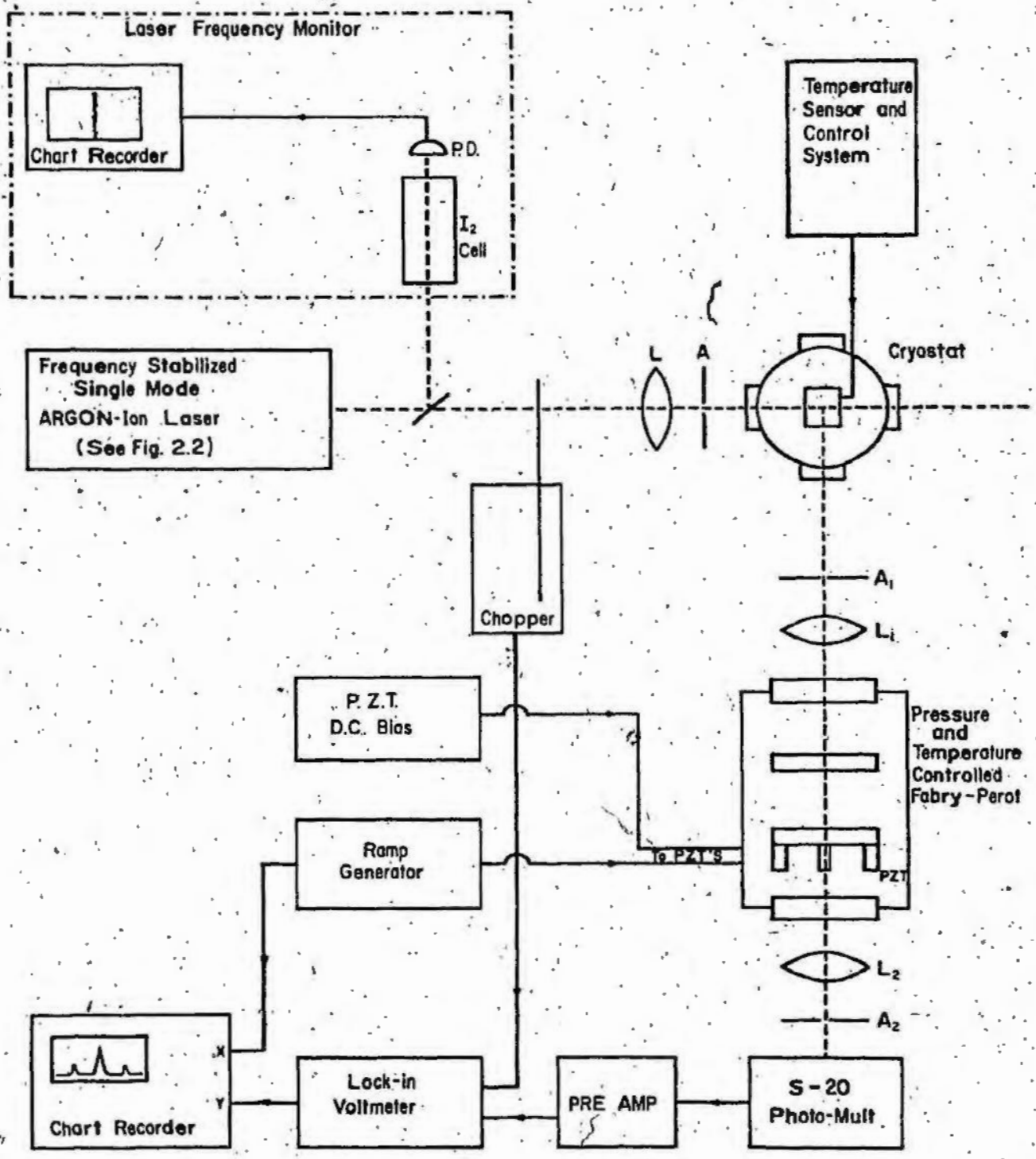
Laser Frequency Monitor
Chart Recorder
P.D.
I_2 Cell
Temperature Sensor and Control System
Frequency Stabilized Single Mode ARGON-Ion Laser (See Fig. 2.2)
L
A
Cryostat
Chopper
A_1
L_1
P.Z.T. D.C. Bias
Pressure and Temperature Controlled Fabry-Perot
Ramp Generator
To PZT's
PZT
L_2
A_2
X
Y
Chart Recorder
Lock-in Voltmeter
PRE AMP
S-20 Photo-Mult

FIGURE 2.1

The light source used in this experiment (see Figure 2.2) was an argon-ion laser (model 52, Coherent Radiation) with principle laser emission of about two watts in the blue-green region of the visible spectrum. The laser was equipped with an intracavity prism (model 431, Coherent Radiation) which permitted selection of any one of several individual lines each with a Doppler broadened width of a few gigahertz.

The laser line at 514.5 nm was used almost exclusively in these experiments because of its relatively high intensity and also because a particularly simple form of frequency control (to be described later) could be used. The axial mode spacing within the Doppler profile of the 514.5 nm line was ~ 115 megahertz and, by using an appropriate intracavity etalon assembly, laser action could be restricted to any one of these modes. In the present case, the etalon (Coherent Radiation) was specially designed to insure maximum mechanical stability by using an annular-shaped "Cervit" spacer between two high quality quartz plates; Cervit having a very low thermal expansion coefficient thus held the plates rigidly parallel at a fixed separation of 1.5 cm (bandpass = 10 GHz) while effectively eliminating thermal expansion effects.

To minimize the problem of laser instability caused by mechanical vibration, the laser was mounted on a specially constructed steel table bearing a large granite block (~ 500 kg) which was effectively isolated from the rest of the structure by rubber mountings. The laser's water cooling lines were equipped with a flow regulator to decrease vibrations and laser temperature changes caused by variations in water pressure.

There were also slow fluctuations and drifts in the laser frequency caused by thermal fluctuations in the cavity structure and,

FIGURE 2.2

Block diagram of the laser frequency stabilizer.

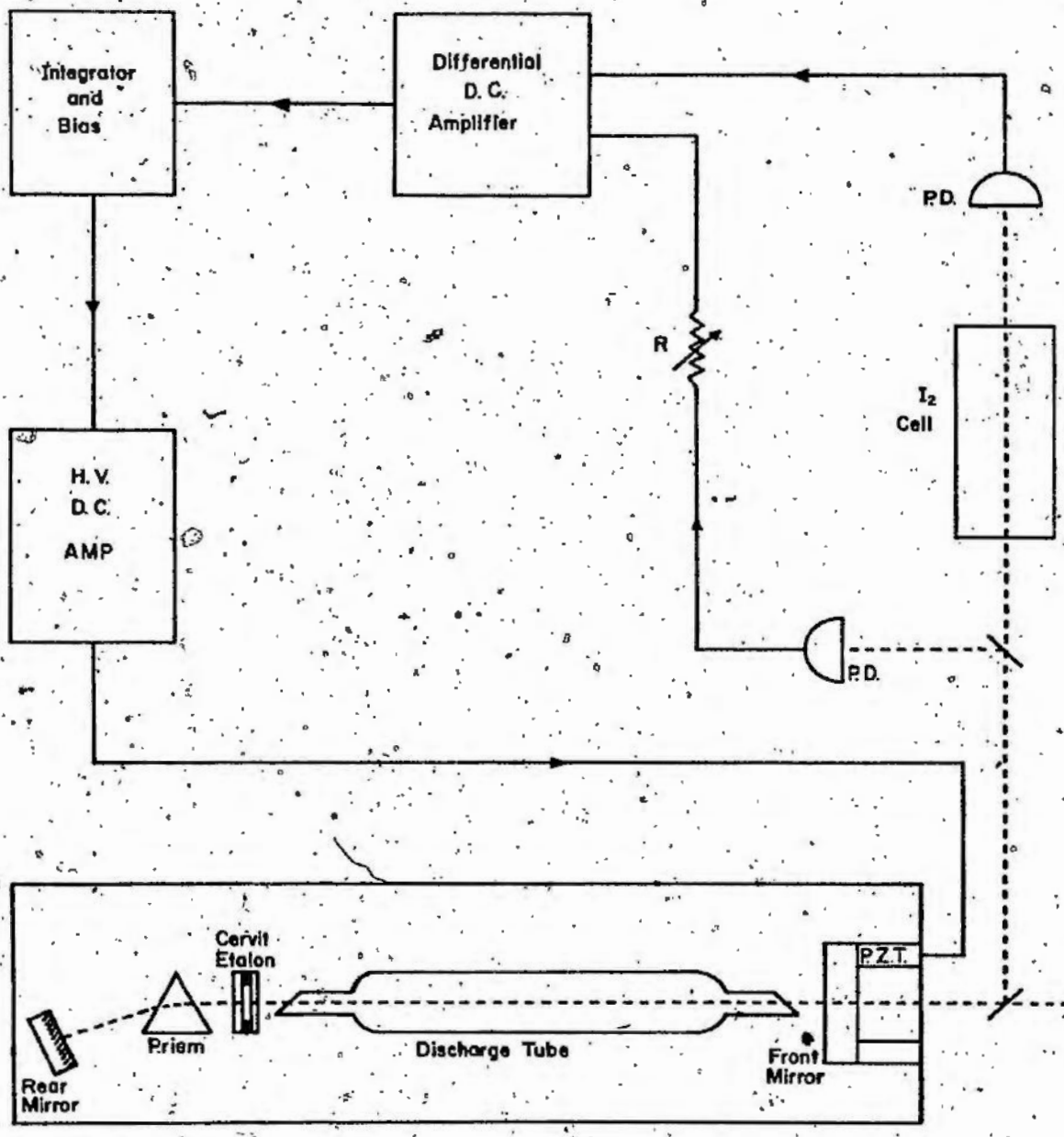
Integrator and Bias
Differential D. C. Amplifier
P.D.
R
I_2 Cell
H.V. D.C. AMP
P.D.
Cervit Etalon
P.Z.T.
Prism
Discharge Tube
Front Mirror
Rear Mirror

FIGURE 2.2

consequently, variations in the refractive index of the laser medium as well as the air in the resonator. These were largely eliminated by means of a specially designed frequency stabilizing device (Hohimer et al., 1972) which had the effect of locking an appropriate cavity mode to the side of the 514.54 nm absorption line of iodine vapour (see Figure 2.2).

Coupling between the laser light and the stabilizer was accomplished by means of beam splitters. Approximately 50% of the diverted light went through a temperature controlled iodine cell and then to a photo-diode, while the remainder went directly to a photo-diode. The two signals were then fed into a differential dc amplifier whose output was integrated, further amplified and then applied to a piezo-electric translator (Tropel model 4500) which supported the laser output reflector. Initial adjustment of the stabilizer involved selecting a laser mode (by manual adjustment of the intracavity etalon) which corresponded to the side of the sharp iodine line so that the most sensitive conversion of frequency fluctuation to intensity fluctuation was achieved. The feedback loop was then closed and any frequency drifts which occurred on a time scale of a few seconds were effectively compensated for by changes in the cavity length resulting from expansion or contraction of the piezo-electric mount.

Using this method, the laser light monitored on a spectrum analyzer (Coherent Optics Inc., Model 470) was kept within 30 MHz for several hours and mode hopping eliminated for intervals of 24-48 hr, after an initial warmup time of several hours.

A second less sensitive but very convenient laser frequency monitor was used continuously during the experiments. It consisted simply

of a second temperature controlled iodine cell whose transmission at the laser frequency was detected by a photo-diode. The output of this diode was fed directly to a strip chart recorder thus providing a permanent record for future reference. The laser beam, with an average power of $\sim$ 100 mW always polarized perpendicular to the scattering plane, was directed into the sample cell by way of a beam-steering device (Jodon Engineering Assoc., Inc., Model BA500A) and brought to a focus at the centre of the cell by a 30 cm quartz lens. The light scattered through 90^{o} from the focus was then collected by a second lens and directed into a Fabry-Perot interferometer.

2.2 Interferometer

Because the Brillouin shift measurements require high resolving power, a Fabry-Perot interferometer (Burleigh, model RC-40) was used. Such an instrument is capable of giving resolving powers of 10^{7}-10^{9} (see Figure 2.3). Basically, it consists of two high precision optical plates separated by a distance d and held parallel to each other. The opposing faces may be flat or identically spherical in geometry and are coated with partially reflecting films. Thus, parallel light incident on one of a pair of flat plates, for example, is reflected back and forth between the plates such that some of the light escapes at each reflection. This multiple reflection between the plates causes constructive or destructive interference and the transmitted light, when focused by a lens, forms an interference pattern of concentric rings in the focal plane of the lens and, for the case of the flat plates, the location of the bright rings is given by the equation:

FIGURE 2.3

The Fabry-Perot Interferometer.

A Aluminum end plate (one of two).

B Invar rod (one of three at 120° spacing).

C Split tube clamp (one of three).

D Movable mirror mount.

E Piezoelectric transducer stack (one of three).

F Mirror ring (accepts premounted mirrors) (one of two).

G Movable mirror.

H Fixed mirror.

I Fixed mirror mount.

K Differential screw (fine adjustment) (one of three).

L Direct drive screw (coarse adjustment) (one of three).

M Differential stabilizer assembly (one of three).

N Lock clamp (activates differential screws) (one of three).

O Aperture (one of two).

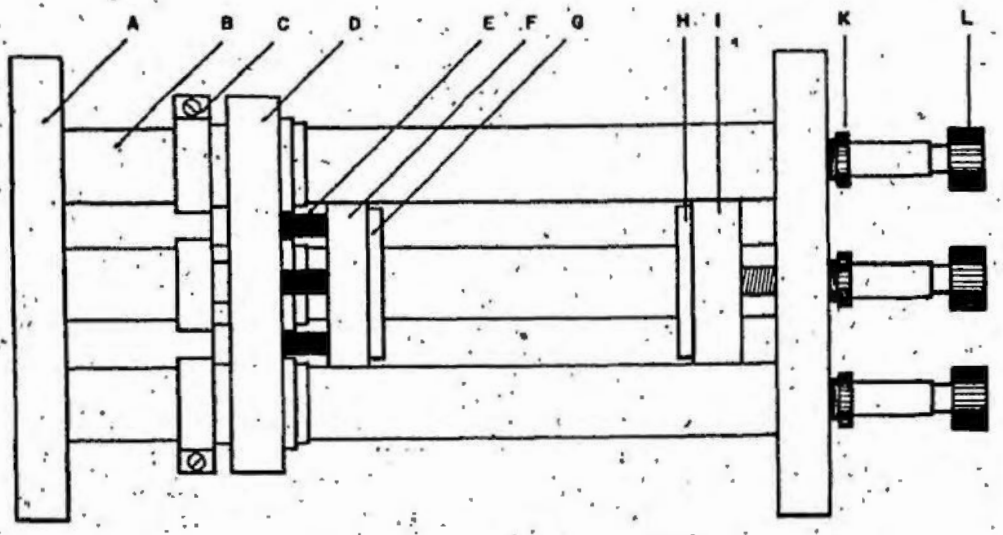

TOP VIEW

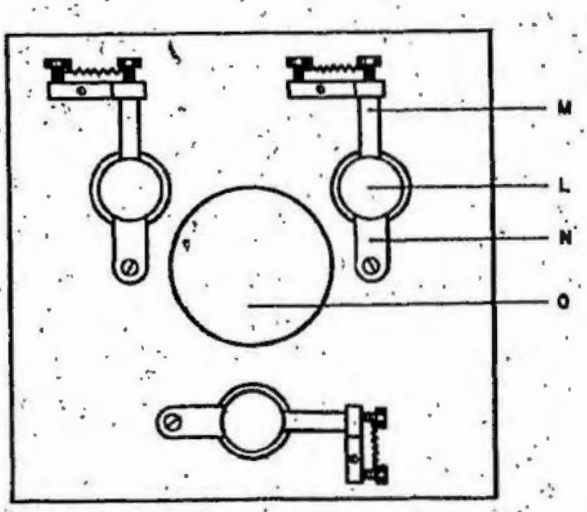

END VIEW

FIGURE 2.3

$$m\lambda = 2nd \cos\theta \qquad (2.1)$$

where m = the order of interference number;

λ = the wavelength of the transmitted light;

n = the refractive index of the medium between the plates;

d = the plate separation;

and θ = the angle between the transmitted beam and the normal to the surfaces.

Considering the light transmitted along the optical axis, $\theta = 0$ and equation (2.1) reduces to

$$m\lambda = 2nd \quad . \qquad (2.2)$$

When matched spherical plates are used, they are normally set in a confocal arrangement where their separation is accurately adjusted to be equal to the common radius of curvature. The condition for constructive interference then becomes:

$$m\lambda = 4d - \rho_m^4/d^3 \qquad (2.3)$$

where d = the axial mirror separation (radius of curvature),

and ρ_m = the radius of the m^{th} bright fringe.

Again, considering only the on-axis transmission, $\rho_m = 0$, and equation (2.3) reduces to:

$$m\lambda = 4d \qquad (2.4)$$

From the relationships between λ and d, we see that by varying the plate separation, d, the order number and the transmitted wavelength corresponding to $\theta = 0$ are changed. This type of "central spot" scanning

(1952); Chase et al. (1964); D'Arrigo and Scott (1967).

was used in the present experiments. A ramp generator (Burleigh, model RC-42) supplied a highly linear, sawtooth waveform to three piezo-electric stacks which supported one of the mirrors at 120° spacings about its circumference. This caused one of the plates to move linearly relative to the other. A "slope trim" adjustment built into the ramp generator provided tilt-free scanning of the interferometer by enabling the slope of the ramp applied to each piezo-electric stack to be varied to compensate for any differences in the response of the stacks.

Thus, by varying the amplitude of the ramp, a number of orders were scanned. A ramp period of 1000 s was normally used with an amplitude of ~ 400 V giving about 5 orders per scan.

The particular arrangement of three piezo-electric stacks was used since they not only provided electronic scanning but also final alignment of the mirrors to $\lambda/250$ parallelism by means of adjustable bias supplies for each stack; the second mirror was mounted on an adjustable mount using three differential screw assemblies which enabled initial alignments to $\lambda/20$ to be made.

The model RC-40 Burleigh Fabry-Perot interferometer was constructed as a solid unit for mechanical stability while all components affecting the cavity spacing were made of Invar because of its low thermal expansion and relatively high mass. The Fabry-Perot mirrors were mounted in Invar mounts by means of Invar tabs epoxied to the outer rim of the mirrors at 120° spacings. They were held rigidly in place by means of three nylon screws which applied a light pressure to the Invar tabs while maintaining the mirrors free from distortion.

To provide greater thermal and mechanical stability to the system, an isolation table and cover were built. This consisted of a welded iron frame (3 m x 1 m x 1 m) elevated from the floor by leveling screws and isolated by rubber pads. The table was covered with a solid birch wood top and weighted down by concrete blocks. A two-meter optical bench was bolted to the centre of the birch top and defined the optic axis of the table.

The interferometer was supported by three point contacts and placed in an air-tight aluminum box which was temperature controlled to $\pm$ 0.5^{o}C to prevent mechanical changes and pressure scanning effects in the Fabry-Perot. The aluminum box was then isolated from the table by rubber mounts at the base of leveling screws. The entrance and exit windows of the box were anti-reflection coated quartz (5 cm diameter).

The whole table containing the interferometer, detector and the associated optics was then covered by a styrofoam box which was 2.5 cm thick and coated with light-proof (black) polyethylene, thus providing further thermal insulation while eliminating stray light contributions. The scattered light entered the box through a small opening in the front end which was equipped with an adjustable aperture A_1*.

The main characteristics of a Fabry-Perot interferometer are its free spectral range, its instrumental bandwidth and its resolving power or finesse.

The free spectral range (FSR), defined as the separation (in frequency or wavelength units) between adjacent transmission maxima, is given by:

---

*See Figure 2.1.

$$\Delta\nu_{FSR} = c/2nd \qquad \text{Plane mirrors} \qquad (2.5)$$
$$\Delta\lambda_{FSR} = \lambda^2/2nd$$

$$\Delta\nu_{FSR} = c/4d \qquad \text{Confocal mirrors} \qquad (2.6)$$
$$\Delta\lambda_{FSR} = \lambda^2/4d$$

where c is the speed of light in a vacuum.

The instrumental bandwidth, defined as the apparent or observed spectral width of a monochromatic spectral line, is given by $\delta\nu$ or $\delta\lambda$.

The finesse, F, of an interferometer, being the fundamental measure of the spectral resolving power of the instrument, is defined as the ratio of the FSR to the instrumental bandwidth, i.e., $F = \frac{\Delta\nu}{\delta\nu} = \frac{\Delta\lambda}{\delta\lambda}$. The finesse of the instrument is determined by a number of factors, the main ones being the reflectivity and surface figure of the mirrors as well as the position, quality and alignment of the optics throughout the system. For perfectly designed plates of reflectivity, R, the reflectivity limited finesse, F_R, is given by:

$$F_R = \frac{\pi\sqrt{R}}{(1-R)} \qquad \text{(Plane mirrors)} \qquad (2.7)$$

$$F_R = \frac{\pi R}{(1-R^2)} \qquad \text{(Confocal mirrors)} \qquad (2.8)$$

In practice, for high R mirrors, the finesse is limited by the smoothness of the mirrors across the aperture used such that, for plates flat to λ/S, a maximum finesse of $\approx S/2$ can be expected. Diffraction of light at the mirror aperture also affects the finesse according to the equation,

$F_D \approx D^2/2\lambda d$, where D is the aperture diameter - this effect being negligible in confocal mirrors. Hence, decreasing the aperture size while increasing the smoothness finesse, significantly increases the diffraction losses thus necessitating a compromise between the two. The contributions to the total finesse, F_T, are combined as parallel impedances; $F_T = (\sum_i (1/F_i))^{-1}$.

Reflectors of both the plane and confocal types were used in the present work. They were high quality quartz plates ≈ 3.8 cm diameter and ≈ 1 cm thick. The plane reflectors offer considerable advantages under conditions where the highest resolution is not required, since the FSR can be adjusted over a wide range by simply changing the plate separation and can be calibrated easily by simply measuring d. These reflectors were therefore used to measure relatively large frequency shifts to, at the outset, establish the absolute scale of frequency shifts by the method of successively reducing the FSR until it could be definitely ascertained that the spectrum was contained within one order of interference. The confocal plates were used primarily for line width measurements because of their characteristically higher resolving power where F >> 100 is possible.

The flat plates had one surface flat to λ/100 and dielectrically coated for a reflectivity of 97% at λ 500 nm over the central 2 cm while the outer surface was anti-reflection coated with a wedge of ≈ 30' relative to the first surface. The plate separation, d, measured with a high precision micrometer, was used in equation (2.5) to calculate the FSR. A lens, L_1*, positioned exactly at its focal length (f_1 = 20 cm)

*See Figure 2.1.

from the scattering site gathered the 90^0 scattered light through the limiting aperture, A_1^* (Diam. ≈ 3 mm), and formed the parallel beam for the Fabry-Perot plates. The limiting aperture, A_1^*, confined the operating aperture of the plates to the central 1 cm diameter and defined the solid angle subtended at the cell centre as ≈ 9.2×10^{-5} steradians.

Lens, L_2^* (f_2 = 60 cm), focussed and centred the interference pattern on a pinhole, A_2^* (Diam. ≈ 400 μ) in front of the detector. The actual size of the pinhole, A_2^*, is a very important factor in deciding the resolution of the system since the range of frequencies $\Delta\nu$ accepted by A_2^* is given from equation (2.1) by

$$\frac{\Delta\nu}{\nu_o} = \frac{\Delta\lambda}{\lambda_o} \simeq \frac{\Delta\theta^2}{2} = 0.5\ (r/f_2)^2$$

where r is the pinhole radius. However, while decreasing r increases the resolving power of the system, it also decreases its light gathering ability; therefore, it was necessary to choose the value of r carefully such that a reasonable compromise was obtained. In the case of the first plates, r was ≈ 200 μ giving a $\Delta\nu$ of ∼ 30 MHz.

The confocal plates were mounted in the same manner as the flat plates but their spacing was necessarily made to coincide with their radius of curvature. Due to their spherical inner surfaces, it was difficult to measure their separation accurately with a micrometer without damaging the delicate inner surfaces; therefore, the free spectral range was determined experimentally by recording a number of Brillouin spectra and calibrating them with respect to the flat-plate spectra obtained under the same experimental conditions. In this way, a FSR of

*See Figure 2.1.

0.9909(0) GHz was obtained for the confocal plates. The outer surfaces of these plates were anti-reflection coated while the inner surfaces were spherical to $\lambda/200$ and dielectrically coated for a reflectivity of 99% at λ 514.5 nm. According to equation (2.7), this would suggest a theoretical finesse, limited mainly by their reflectivity, of $F_R \approx 150$.

Alignment of the Fabry-Perot was performed by analyzing the laser light scattered from a white card placed immediately in front of the scattering cell while observing the detector output on an oscilloscope (Tektronix, Inc., model 7704): a beam splitter, placed in the incident laser beam, redirected approximately 5% of the light onto the card using a converging lens to focus it to a point on the card which was coincident with the axis of the scattering optics. Lens L_1^* was positioned at its focal length from the card and transmitted the scattered light to the interferometer. With the Fabry-Perot scanning at a fast rate, the transmitted signal observed on the scope was first optimized by manually adjusting the position and alignment of the plates via the differential screw assemblies mentioned earlier. The final alignment was performed electronically by adjusting the bias on the individual piezo-electric stacks until a maximum finesse was observed, and this was not attempted until the instrument had been sealed in its temperature controlled aluminum container for a day or more.

A theoretical finesse of ~ 35 could be expected for the flat ($\lambda/100$) plates (limited mainly by their surface irregularities) and ~ 150 for the confocals (reflectivity limited finesse), the best operating finesses achieved were approximately 30 and 60 for the flat and

*See Figure 2.1.

confocal plates, respectively. The former figure was considered acceptable because of the difficulty of maintaining the flat plates in accurate alignment. A finesse of 60 for the spherical plates was considered low, however, since these plates are relatively insensitive to misalignment and finesses in excess of 100 are commonly achieved. Careful investigation, in fact, revealed that the observed finesse in the latter case was not determined by the optical quality of the Fabry-Perot reflectors, but rather by frequency fluctuations ('jitter') in the laser output. These fluctuations of up to 20 MHz occurred at intervals (0.1 s or less) considerably shorter than the time required to sweep through a spectral line at the normal rate, and the response time of the frequency stabilizer was too long to compensate for these effects. In order to obtain a higher effective finesse and resolving power, it would have been necessary to acquire a more stable laser and/or a data collection system based on photon counting techniques whereby (1) the spectrum is repetitively scanned in periods of 1 s or less with the information being stored in a multichannel scalar and (2) special provision is made for electronically locking the strong central component of the spectrum to a particular reference channel in the scalar. However, the resolving power of $\sim 10^7$ already attained was adequate for the determination of Brillouin line widths over most of the liquid ranges in O_2 and N_2, so it was decided not to delay the project while these extensive improvements were undertaken.

2.3 Photomultiplier Tube and Detection System

The detector used in this experiment was an ITT model FW-130 photomultiplier tube (PMT) having S-20 spectral response characteristics. The most important features of the tube were its relatively high sensitivity and low dark count rate. The low dark count was due mainly to the tube's small photocathode area (~ 0.25 cm diam.) which was specially designed for cases where the incident light can be focused to a near spot. This effectively increases the S/N ration that would be otherwise attainable from a similar tube with a larger photocathode by decreasing the number of possible thermionic emissions.

The dark count rate and tube noise were further reduced by installing the tube in a refrigerated chamber (model T.E. 104-RF, Prod. for Research). This thermoelectrically cooled, RF-shielded chamber automatically controlled the cathode temperature to $\sim -20^{o}C \pm 0.5^{o}C$. Light passing through the pinhole, A_2 (Figure 2.1), was focused on the small cathode surface via a short focal length lens (f = 7 cm) installed in the front end of the RF chamber.

A Brower Laboratories Model 261 preamplifier was used to amplify the low level signals from the PMT, while providing impedance-matching between the tube and the lock-in voltmeter (model 131, Brower Laboratories, Inc.). To prevent stray pickup in the leads, the preamp was placed as near as possible to the PMT.

A chopper placed in the laser beam before it entered the cell provided a reference frequency for the lock-in voltmeter. The lock-in voltmeter thus amplified only the signal from the preamplifier which was

in phase with the chopper frequency. This phase sensitive detection thus filters out most of the random noise from the tube while retaining the relevant signal for further amplification. The resulting dc signal was then recorded on a linear chart recorder (Sargeant model SRL).

The time constant of the Brower lock-in unit was set in conjunction with the scanning rate to reduce the instrumental line-pulling effects on the recorded spectra. It was found that, for a single scan time of 1000 seconds, a 3-second time constant was appropriate for the frequency shift measurements while, for line width studies, it was necessary to decrease it to 1 second.

2.4 Cell and Gas Handling System

The scattering cell used in these experiments (see Figure 2.4) was specially designed by M. J. Clouter and H. Kiefte to withstand the large temperature and pressure variations involved. The cell was made from a BeCu alloy in the shape of a cube (≃ 2.5 cm), the miniaturized design being used to minimize thermal gradients in the cell. The scattering volume was located at the intersection of three mutually perpendicular holes, two horizontal (3.2 mm diam.) and one vertical. The four openings in the horizontal holes were then sealed by quartz windows (Q) (10 mm diam. x 3.2 mm thick) using an indium O-ring seal. Two of these windows were used to direct the laser beam straight through the cell; a lens, L*, focused at the centre of the cell, collected the 90° scattered light through a third window and transmitted it to the interferometer, while the fourth window was used for visual observation of the samples and alignment purposes. A small stainless steel tube, I

*See Figure 2.1.

FIGURE 2.4

The Scattering Cell (vertical section)

I Gas inlet tube.

P Brass post (one of two).

F Free gap.

Q Quartz window.

G Epoxy resin cement.

Cu Copper foil.

In Indium solder.

Wp BeCu window plate.

O Indium O-ring.

T_1 Platinum thermometer well.

T_2 Secondary thermometer well (not used in present experiments).

The control thermometer (GaAs not shown) was located on the front face of the cell between the posts P.

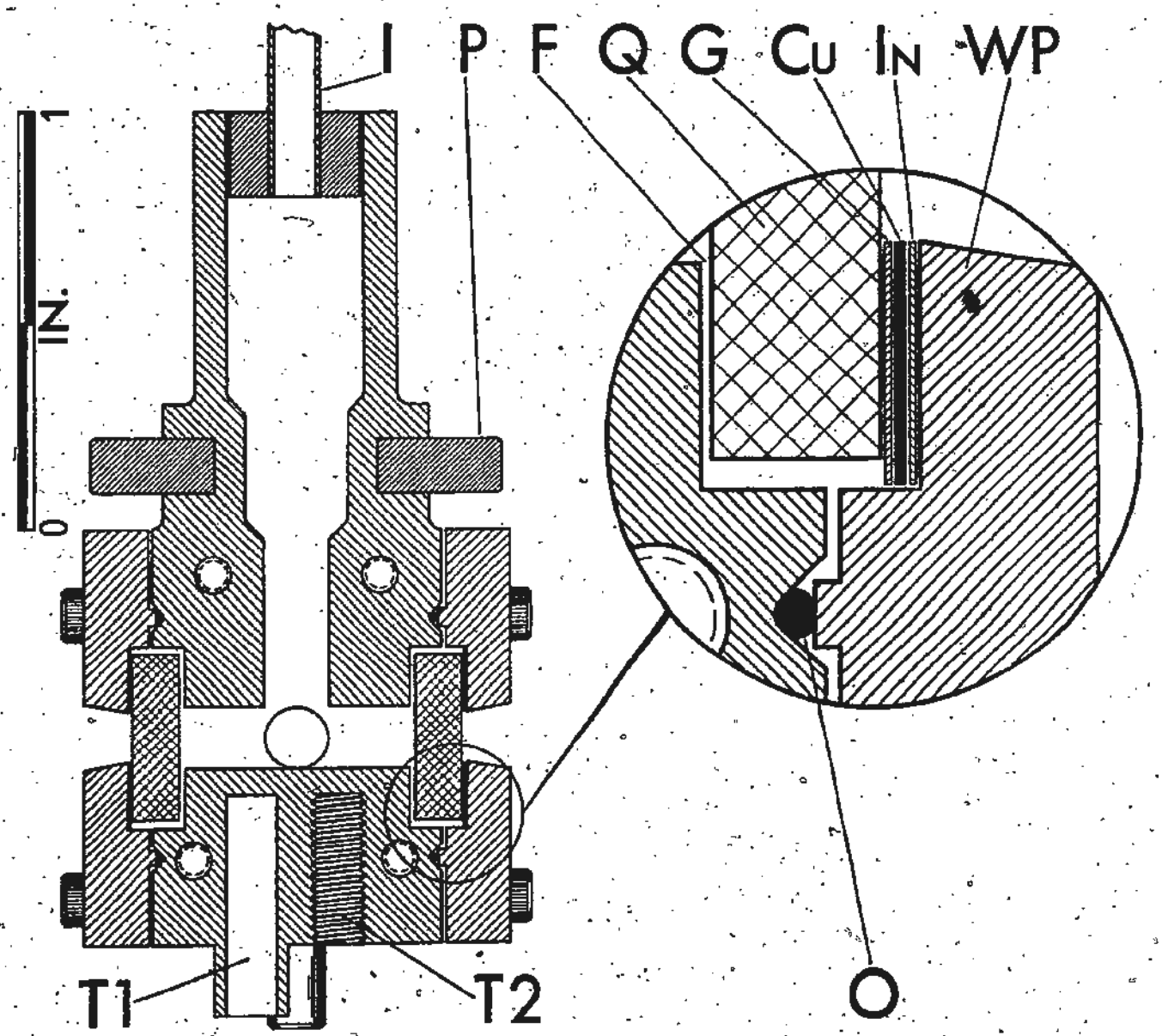

FIGURE 2.4

(3.2 mm diam., 0.15 mm wall), was hard soldered into the top of the cell to seal the vertical hole while providing communication with the gas handling system.

Thermal contact between the cell and the cryostat was made by two copper braids ~ 5 cm long which were soldered to a heat sink at the base of the heat exchange column of the cryostat, and the other ends were fastened to two posts (P) (180^{o} apart) at the top of the cell. Electrical heaters of 25 ohms each were wound on the posts and connected in series; a GaAs thermometer, T_1, used as a control thermometer, was mounted on the cell close to the heaters to minimize thermal-lag effects. These were connected in a feedback circuit to automatically control the temperature of the cell.

A platinum resistance thermometer, T_2, was mounted on the cell as close as possible to the scattering site. This thermometer, which was calibrated (Cryogenic Calibrations, Pitchott, England) according to the International Practical Temperature scale (1968) to a claimed accuracy of ± 8 mK, was used to obtain the absolute temperature measurements of the sample. These measurements were made on a null detector (Fluke, model 891A) immediately before and after each spectrum was recorded to check against possible thermal drifts. To ensure that thermal equilibrium had been established in the cell, its temperature was automatically controlled for about 2 h at each setting before the final readings were taken.

The cell inlet tube, I, was externally connected to the high-purity gas reservoir as well as a series of three Bourdon-tube gauges and a rupture-disc pressure fuse. The Bourdon-tube gauges were used to

measure the vapour pressures of the liquid samples accurately (0.2% to 0.5%) and these measurements were used as a check against the temperature measurements obtained via the platinum thermometer.

To prevent contamination of the sample by dust particles and other impurities, the gas handling system and the cell were rinsed repeatedly with a variety of filtered liquids before assembly. After being assembled, the whole system was evacuated and flushed several times with oxygen gas at room temperature to oxydize any remaining impurities before admitting the gas sample (Matheson Gas Products, 99.99% pure). Any remaining dust particles in the cell were allowed to settle to the bottom before spectra were taken.

2.5 Cryostat.

The scattering cell, supported by the gas inlet tube, was placed in the tail section of a variable temperature Cryostat (Andonian Associates, model IV-4-0500) to form the liquid samples (see Figure 2.5). The gas-inlet tube, I, passed vertically through the middle of the cryostat using point contacts of triangular teflon spacers for centering. The inlet tube entered the cryostat at the top through a vacuum O-ring seal whose flexibility permitted some vertical and rotational adjustments to the cell for alignment purposes. An annular exchange gas chamber, G, surrounded the inlet tube and was insulated from it by a vacuum space. The base of the exchange gas column was closed by a relatively large brass ring, M, which served as a heat sink for the system. The exchange gas chamber was surrounded in turn by two concentric, liquid coolant reservoirs which were also separated from each other by a vacuum space (H).

FIGURE 2.5

The Cryostat.

A Electrical feedthrough.

B Exchange gas port.

C Nitrogen fill and vent.

D Nitrogen vent.

E Nitrogen fill.

F Nitrogen reservoir (outer).

G Exchange gas chamber.

H Vacuum gap.

I Sample support tube.

J Nitrogen reservoir (inner).

K Outer tail section.

L Nitrogen temperature radiation shield.

M Heat sink.

N Sample cell.

O Quartz window (one of four).

P Copper braids.

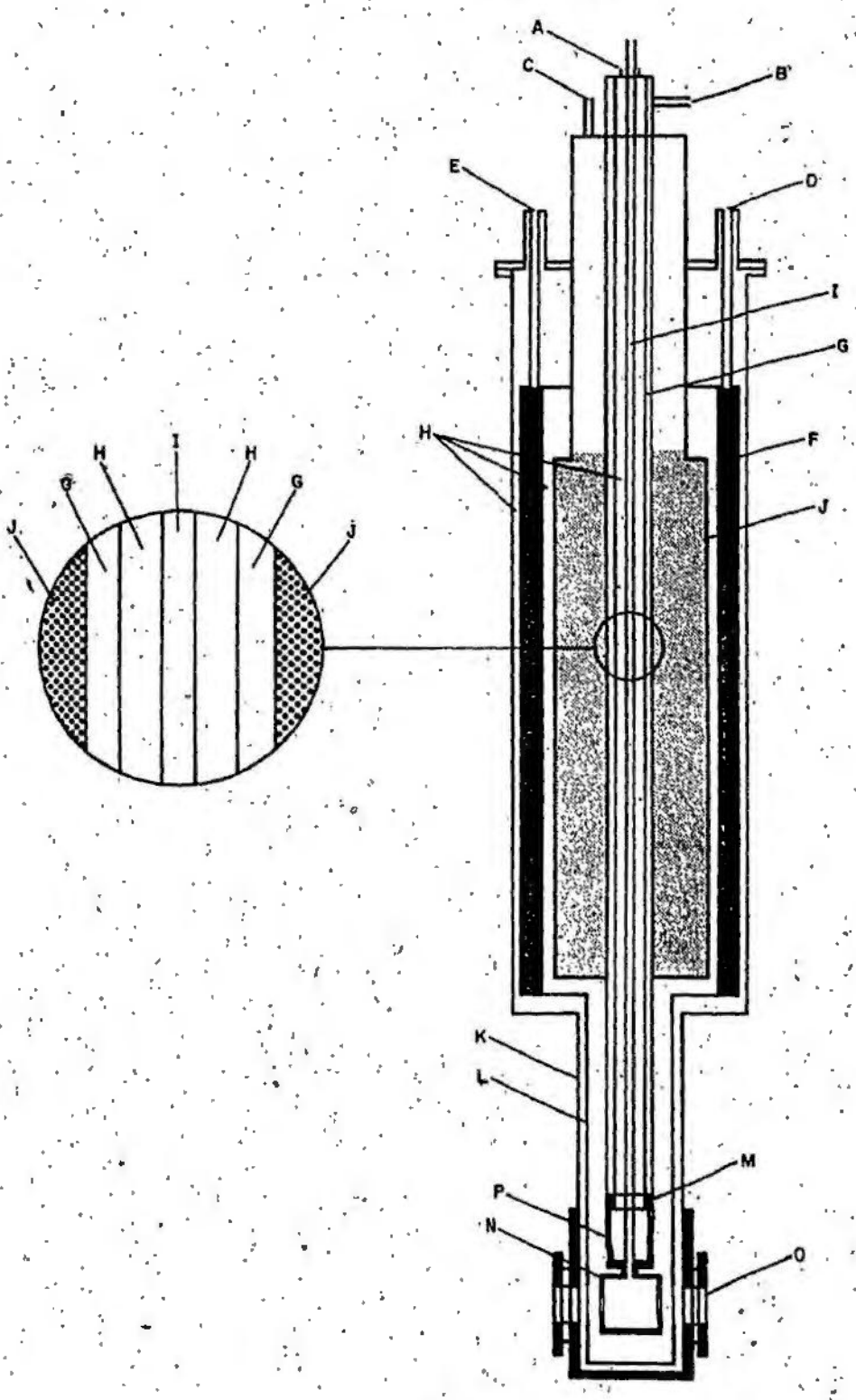

FIGURE 2.5

The inner reservoir, J, shared a common wall with the exchange gas chamber through which thermal contact between the coolant and the exchange gas was attained. The outer reservoir, F, was also insulated from the laboratory environment by a vacuum space between it and the outer shell of the cryostat. Four quartz windows (O) (3 cm diam. x 0.3 cm thick) were mounted on the tail section, K, to correspond to the cell windows.

The internal volume of the cryostat was evacuated to $\sim 10^{-5}$ torr by a portable vacuum system (Alcatel model 5477) and the liquid coolant reservoirs filled with the appropriate coolant; liquid nitrogen was used for N_2 and O_2 samples over the temperature ranges considered. Oxygen gas was admitted into the evacuated exchange gas column to provide the necessary thermal link between the liquid coolant and the sample site via the heat sink; i.e., O_2 gas condensing on the cold wall of the liquid N_2 reservoir, J, falls to the heat sink, M, to which the cell's cooling braids (P) are connected. Upon evaporating, the O_2 droplets absorb heat from the sink thus lowering its temperature.

The amount of cooling power thus provided to the cell was controlled by varying the amount of O_2 gas in the exchange column. Using this method, temperatures down to $\sim$ 80 K were easily obtained, while lower temperatures of $\sim$ 70 K were achieved by lowering the temperature of the coolant itself by lowering its vapour pressure via a vacuum pump.

The complete cryostat as described, with the scattering cell in position, was vertically suspended above the floor on a metal frame and carefully aligned to allow the laser beam to pass through the centre of the cell undeflected.

2.6 Analysis Procedures

Using the experimental setup thus described, at least ten spectral orders were scanned at each temperature setting for the liquid O_2 and N_2 samples, and the results permanently recorded on chart paper. The centre of each spectral line was carefully located, through which a straight line was drawn to represent its central frequency. The relative separations (measured from these predetermined line centres) between the Rayleigh lines and their corresponding Brillouin lines, as well as between consecutive Rayleigh lines (i.e., interorder spacing), were measured directly with a linear scale. The Brillouin shifts, expressed as a fraction of the FSR, were then obtained as the quotient of the relative Rayleigh-Brillouin separations to the corresponding interorder spacings. These quotients were then averaged over all the orders scanned for each spectrum, the mean values of which were multiplied by the FSR of the interferometer to obtain the Brillouin frequency shifts in GHz.

A similar procedure was followed for the determination of the recorded full width at half-maximum (FWHM) of the Brillouin lines; the half-maximum points were taken midway between the peak maximum and the interorder intensity minimum for each Brillouin line. Once the half-maximum points were determined, the full widths of the individual lines were measured at these points and expressed as fractions of the interorder spacings. These fractions were then averaged over all the spectral orders recorded for each spectrum with the mean value again being multiplied by the FSR to determine the FWHM ($\Delta_{B_{obs}}$) of the observed Brillouin line width in MHz.

In cases where linepulling effects were present (mainly near the critical points where the Rayleigh intensity becomes relatively high), efforts were made to reconstruct the true line shapes by subtracting the overlapping wings directly using graphical superposition techniques before measurements of frequency shifts or line widths were attempted. These linepulling effects ultimately limited how accurately the spectral lines could be resolved as the critical points were approached. At one time, efforts to approach the critical point more closely using the blue line of the laser (λ = 488.0 nm) were attempted, but the results obtained were considered inconclusive due to suspected leaks in the gas handling system which made the sample purity questionable.

Coincidentally with the latter problem a leak also developed between the atmosphere and the main vacuum space of the cryostat which led to thermal instabilities at the sample site and an extremely high coolant consumption. Unfortunately, it was found that the possible solution to this problem involved extensive repairs to the cryostat and it was consequently decided to terminate this stage of the project without further investigating the critical region.

CHAPTER 3

EXPERIMENTAL RESULTS

Figures 3.1 and 3.2 show typical Brillouin spectra which were obtained for nitrogen and oxygen; their variations with temperature are also shown. These spectra show the central Rayleigh components at the laser emission frequency as well as the Stokes and anti-Stokes shifted Brillouin components as predicted by the Brillouin equation (1.3).

Scattering theory further predicts that the true spectral lines are very nearly Lorentzian in shape (McIntyre and Sengers (1968)) with a relative intensity given by the Landau-Placzek relation as

$$I_R/2I_B = \gamma - 1 \qquad (3.1)$$

where $\gamma = C_p/C_v$ is the ratio of the specific heats, and I_R and I_B are the absolute intensities of the Rayleigh and Brillouin lines, respectively; the latter being given by (Wong and Anderson (1972)):

$$I_B \propto (n^2 - 1)T\kappa_s \qquad (3.2)$$

where n is the index of refraction;

T is the absolute temperature;

and κ_s is the adiabatic compressibility.

However, the actual recorded intensity of the individual spectral lines was found to depend greatly on the experimental setup used to record them. The factors affecting the recorded intensity were unavoidable stray light (mainly from parasitic scattering in the

FIGURE 3.1

Brillouin spectra of saturated liquid nitrogen.
a, b, c, and d were recorded using flat plates
with a FSR = 3.400(1) GHz,
e was recorded using the confocal mirrors
with a FSR = 0.9909(0) GHz.

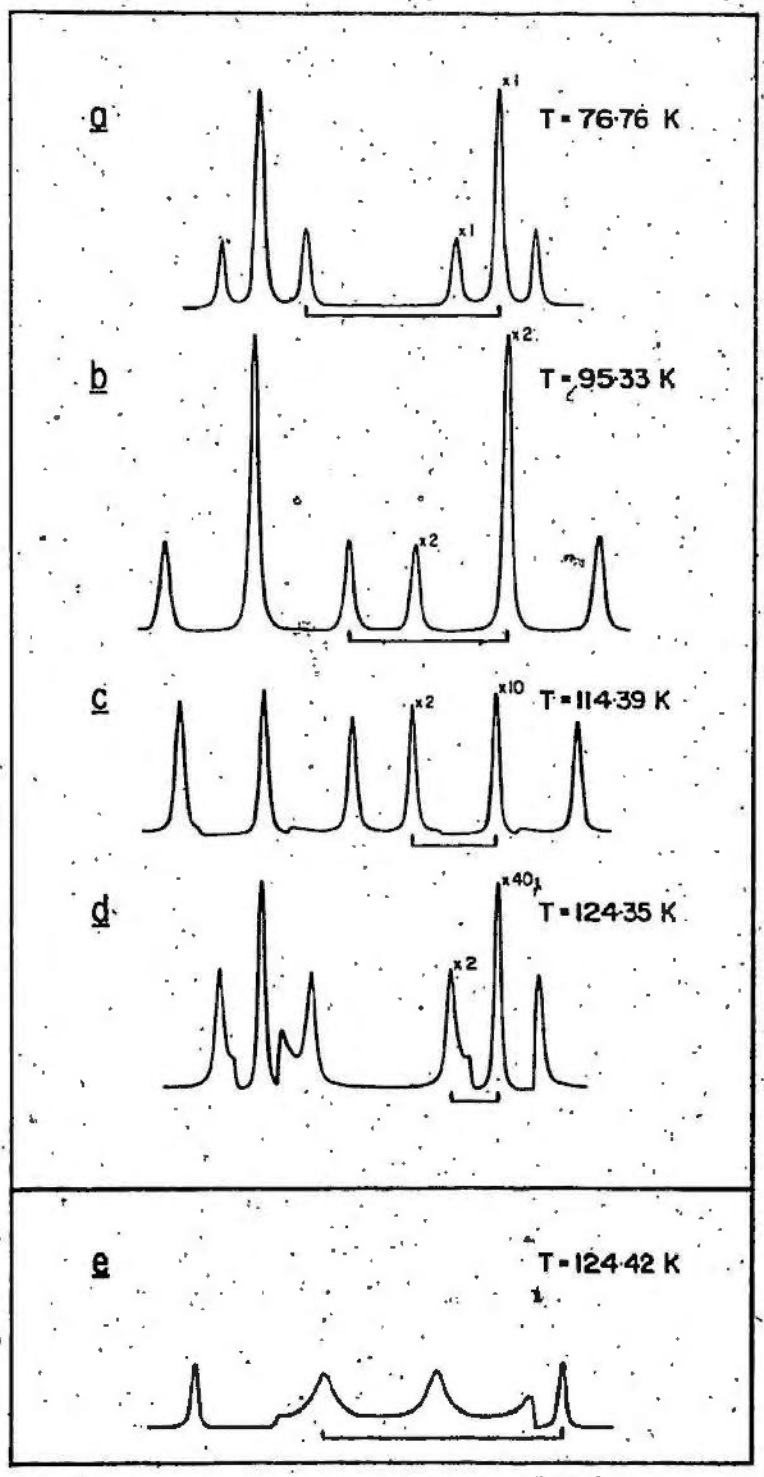
a
T = 76·76 K
x1
x1
b
T = 95·33 K
x2
x2
c
T = 114·39 K
x2
x10
d
T = 124·35 K
x2
x40
e
T = 124·42 K

FIGURE 3.1

FIGURE 3.2

Brillouin spectra of saturated liquid oxygen.
a, b, and c were recorded with a FSR = 13.05(1) GHz,
d was recorded with a FSR = 2.937(5) GHz.

*See Figure 2.1.

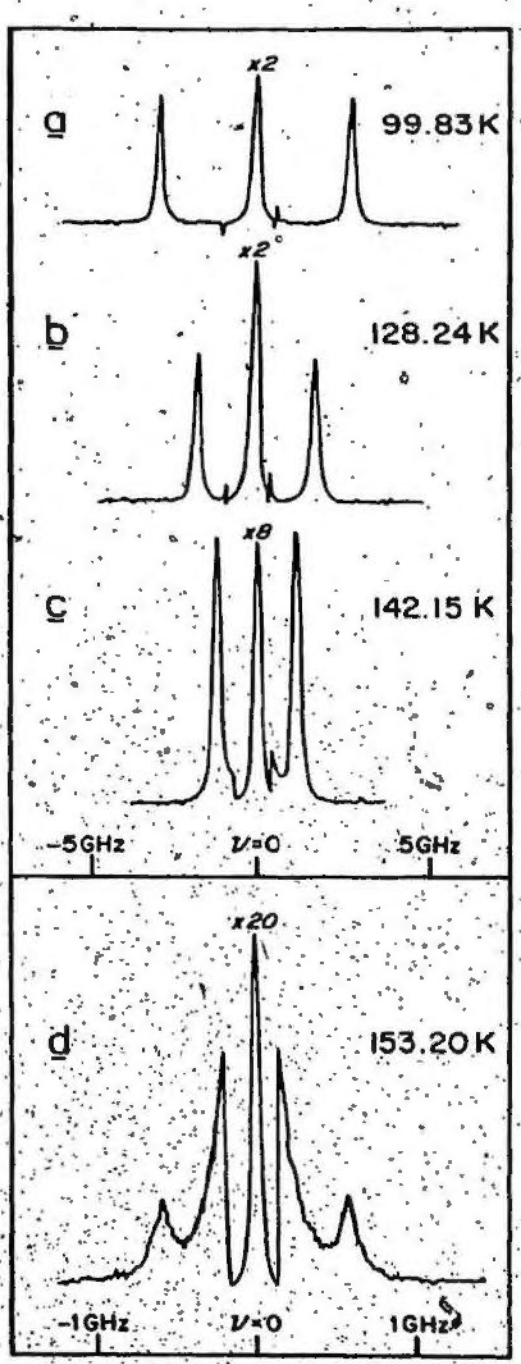

FIGURE 3.2

cell) which contributed to the intensity of the Rayleigh components, variations in the power of the incident laser beam (long-term fluctuations were significant) while the overall intensity of the spectra was found to depend critically on the alignment of the scattering optics, with minor variations in alignments causing major changes in the overall intensity. For these reasons, no attempts were made to measure the absolute intensity of the various lines and, therefore, the validity of equations (3.1) and (3.2) was not investigated in this research. However, in earlier work (Clouter et al. (1975)) done on oxygen, where special precautions were taken in the alignment of the scattering optics and in the reduction of stray light contributions, the Landau-Placzek relation was investigated; the results are presented in Appendix A.

3.1 Determination of Velocities

The hypersonic velocities were calculated directly from the observed Brillouin shifts using the equation:

$$\Delta\nu_i = \nu_s = \frac{2nV}{\lambda_i} \sin\left(\frac{\theta}{2}\right) \qquad (3.3)$$

where $\Delta\nu_i = \nu_s$ is the measured Brillouin frequency shift;

n is the index of refraction;

λ_i is the wavelength of the incident radiation;

V is the phase velocity of the acoustic wave at the frequency ν;

and θ is the scattering angle which was adjusted to $90.0(0)^\circ$ throughout this experiment.

The hypersonic velocities thus obtained for saturated liquid oxygen and liquid nitrogen, from their normal boiling points (T_{nbp}) to their critical points (T_c), are presented in Tables 3.1 and 3.2 along with corresponding (interpolated) ultrasonic results as obtained from the literature. Graphs of velocity versus temperature are also given in Figures 3.3 and 3.4. Results for oxygen in the temperature range below the normal boiling point (T_{nbp} = 90.19 K) are also presented in Appendix A for completeness.

Index of refraction data corresponding to $T_{nbp} < T < T_c$ were not available for either liquid nitrogen or liquid oxygen so the values used, as listed in Tables 3.1 and 3.2, were obtained from the Lorentz-Lorenz relation:

$$L = \frac{n^2 - 1}{n^2 + 2} \rho^{-1} \qquad (3.4)$$

where the quantity, L, is assumed a constant which can be determined from knowing the value of the index of refraction, n, and the corresponding density, ρ, for at least one temperature value. Data given by Johns and Wilhelm (1937), at λ = 546.1 nm and λ = 435.8 nm, were interpolated for the laser wavelength of λ = 514.5 nm used in this research to get values of n in the temperature ranges below the normal boiling points of the liquids. These values were then used in conjunction with density data from Weber (1970) for oxygen and Roder et al. (1968) for nitrogen to find L. This value of L was then used to calculate further values of n for temperatures $T_{nbp} < T < T_c$ using equation (3.4), and further density data from Weber (1970) and Roder et al. (1968).

TABLE 3.1

Brillouin scattering data and corresponding ultrasonic velocities for saturated liquid oxygen*

Temperature T(K)	Frequency Shift $\Delta\nu_i$ (GHz)	Refractive Index n	Hypersonic Velocity V (ms^{-1})	Ultrasonic Velocity V (ms^{-1})
Flat Plates, FSR = 13.051 GHz				
86.66	3.174	1.2289	939.7	934.4
99.83	2.767	1.2150	828.6	824.8
106.30	2.562	1.2078	771.8	767.5
114.46	2.298	1.1979	698.0	693.0
121.28	2.053	1.1890	628.2	628.8
128.24	1.793	1.1789	553.4	557.8
135.68	1.522	1.1664	474.8	474.2
139.87	1.343	1.1583	421.9	423.4
141.38	1.284	1.1550	404.5	404.1
142.15	1.240	1.1533	391.2	393.9
145.32	1.099	1.1455	349.1	350.7
147.68	0.978	1.1386	312.5	314.7
Flat Plates, FSR = 2.9375 GHz				
139.70	1.369	1.1586	430.0	425.5
145.60	1.083	1.1448	344.2	346.8
149.17	0.8821	1.1336	283.1	288.6
149.29	0.8815	1.1332	283.0	286.5

TABLE 3.1, continued

Temperature T(K)	Frequency Shift $\Delta\nu_j$ (GHz)	Refractive Index n	Hypersonic Velocity V (ms^{-1})	Ultrasonic Velocity V (ms^{-1})
Flat Plates, FSR = 2.9375 GHz				
150.84	0.7799	1.1265	251.9	259.6
151.95	0.7021	1.1206	227.9	240.0
151.97	0.6982	1.1205	226.7	239.6
152.66	0.6345	1.1170	206.7	225.9
153.20	0.6063	1.1136	198.1	214.7
153.37	0.5922	1.1123	193.7	210.9
153.51	0.5678	1.1108	186.0	207.3
153.77	0.5437	1.1083	178.5	200.4
153.90	0.5276	1.1065	173.5	197.0
154.04	0.4956	1.1049	163.2	—
154.06	0.4826	1.1045	159.0	—

*The ultrasonic data was interpolated from the results of Van Daël et al (1966).

TABLE 3.2

Brillouin scattering data and corresponding ultrasonic velocities for saturated liquid nitrogen*

Temperature T(K)	Frequency Shift $\Delta\nu_i$ (GHz)	Refractive Index n	Hypersonic Velocity V (ms^{-1})	Ultrasonic Velocity V (ms^{-1})
Flat Plates, FSR = 3.4001 GHz				
72.94	2.966	1.2048	895.8	894.8
76.76	2.829	1.2003	857.4	856.8
80.94	2.678	1.1953	815.2	814.5
83.28	2.592	1.1924	790.9	790.0
85.82	2.488	1.1891	761.2	763.5
88.05	2.409	1.1862	739.0	740.7
90.43	2.313	1.1831	711.2	714.4
92.82	2.225	1.1798	686.1	687.8
95.33	2.124	1.1762	657.1	659.2
97.58	2.042	1.1729	633.3	631.1
99.95	1.937	1.1694	602.7	604.9
101.89	1.862	1.1663	580.7	581.0
103.95	1.772	1.1629	554.4	555.4
105.54	1.706	1.1602	534.8	534.6
107.71	1.613	1.1563	507.6	506.3
109.60	1.520	1.1528	479.6	481.1
111.94	1.411	1.1481	447.1	448.2

TABLE 3.2, continued

Temperature T(K)	Frequency Shift $\Delta\nu_i$ (GHz)	Refractive Index n	Hypersonic Velocity V (ms^{-1})	Ultrasonic Velocity V (ms^{-1})
Flat Plates, FSR = 3.4001 GHz, continued				
114.39	1.290	1.1427	410.6	412.0
116.62	1.160	1.1373	371.1	376.4
118.78	1.042	1.1314	335.0	338.1
120.98	0.9051	1.1243	292.9	289.8
123.13	0.7495	1.1158	244.4	248.6
124.35	0.6419	1.1095	210.5	218.9
Confocal Plates, FSR = 0.9909(0) GHz.				
103.75	1.788	1.1632	559.3	558.0
105.06	1.728	1.1610	541.4	540.9
107.54	1.617	1.1567	508.4	508.6
114.45	1.287	1.1426	409.8	411.1
115.99	1.202	1.1389	384.1	386.7
116.95	1.165	1.1365	373.0	371.0
118.01	1.115	1.1336	357.8†	352.0
121.49	0.8782	1.1225	284.6	284.6
121.97	0.8657	1.1207	281.0†	274.9
122.58	0.8097	1.1182	263.4	262.1
123.14	0.7575	1.1157	247.0	248.4

TABLE 3.2, continued

Temperature T(K)	Frequency Shift $\Delta\nu_i$ (GHz)	Refractive Index n	Hypersonic Velocity V (ms^{-1})	Ultrasonic Velocity V (ms^{-1})
Confocal Plates, FSR = 0.9909(0) GHz				
123.74	0.7092	1.1128	231.8	233.8
124.09	0.6777	1.1111	221.9	225.2
124.42	0.6495	1.1091	213.1	216.6
124.90	0.6022	1.1063	198.1	200.0
125.20	0.5674	1.1044	186.9	190.1
125.29	0.5533	1.1037	182.4	187.8
125.37	0.5473	1.1032	181.4	186.1
125.47	0.5413	1.1024	178.7	183.7
125.52	0.5361	1.1021	177.0	182.5
125.63	0.5261	1.1012	173.8	—
125.68	0.5156	1.1008	170.4	—
125.70	0.5117	1.1006	169.2	—
125.79	0.5072	1.0999	167.8	—
125.84	0.4954	1.0994	163.9	—
125.89	0.4955	1.0990	164.0	—

*The ultrasonic data were interpolated from the results of Van Dael et al. (1966).

†Possible increased uncertainty due to linepulling effects.

FIGURE 3.3

Plot of sound velocity vs. temperature for saturated liquid oxygen. The triangles represent hypersonic (0.4 to 5 GHz) velocities. The experimental error in these measurements is less than 0.5% near T_{nbp} and increases gradually to $\sim$ 1% near T_c. The solid curve represents the ultrasonic (1.2 MHz) velocities as measured by Van Dael et al. (1966) with a claimed accuracy of less than 0.05%.

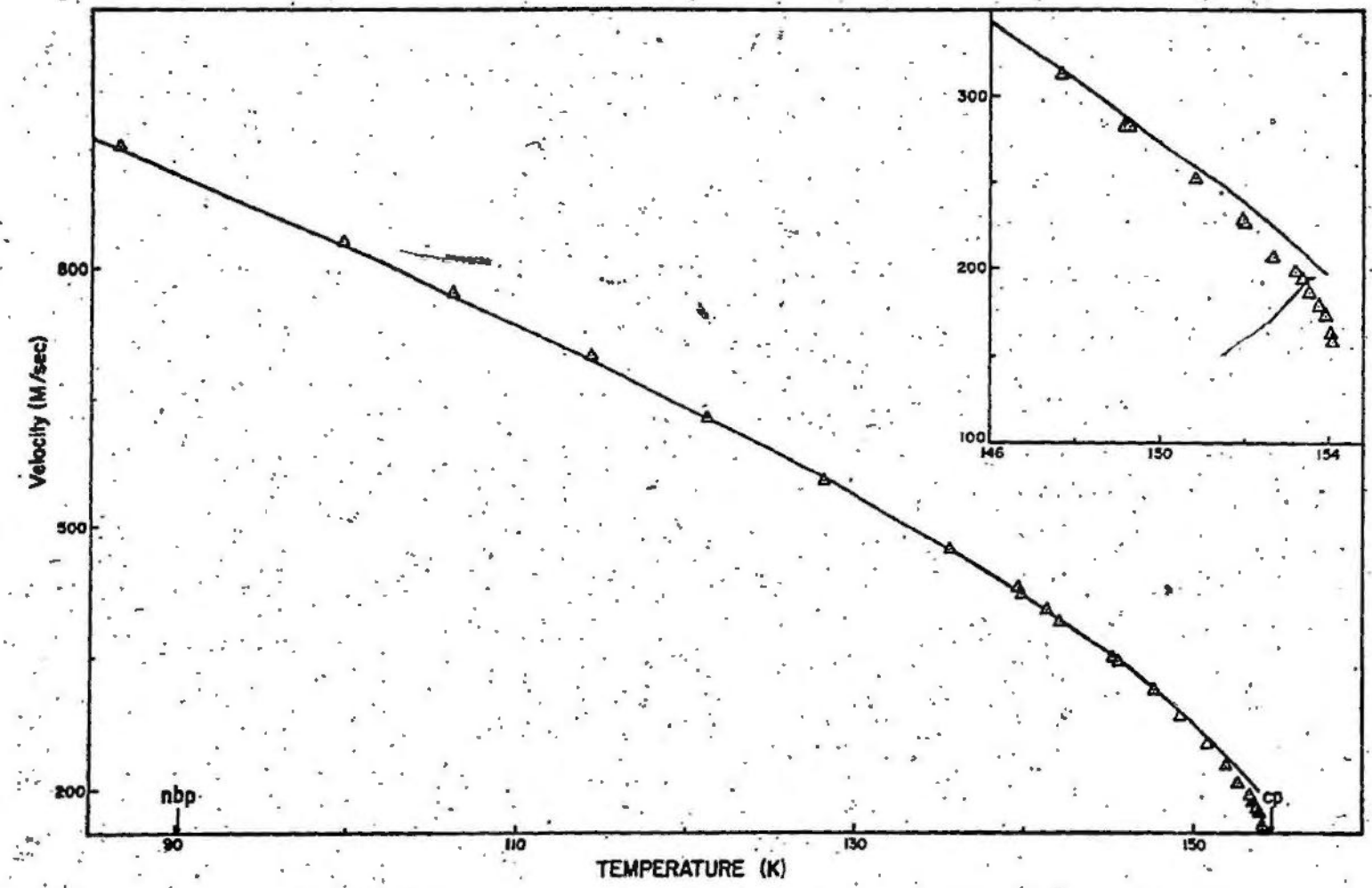
Velocity (M/sec)
800
500
200
nbp
90
110
130
150
TEMPERATURE (K)
cp
300
200
100
146
150
154

FIGURE 3.3

FIGURE 3.4

Plot of sound velocity vs. temperature for saturated liquid nitrogen. The triangles represent Hypersonic (0.4 - 5 GHz) velocities obtained in the present experiments with an experimental error of less than 0.5% near T_{nbp} and increasing gradually to less than 1% near T_c. The dots represent hypersonic (3 - 5 GHz) velocities as measured by Pine (1969) to a claimed accuracy of 0.1%, while the solid curve represents the ultrasonic (1.2 MHz) velocities as measured by Van Dael et al. (1966) with a claimed accuracy of less than 0.05%.

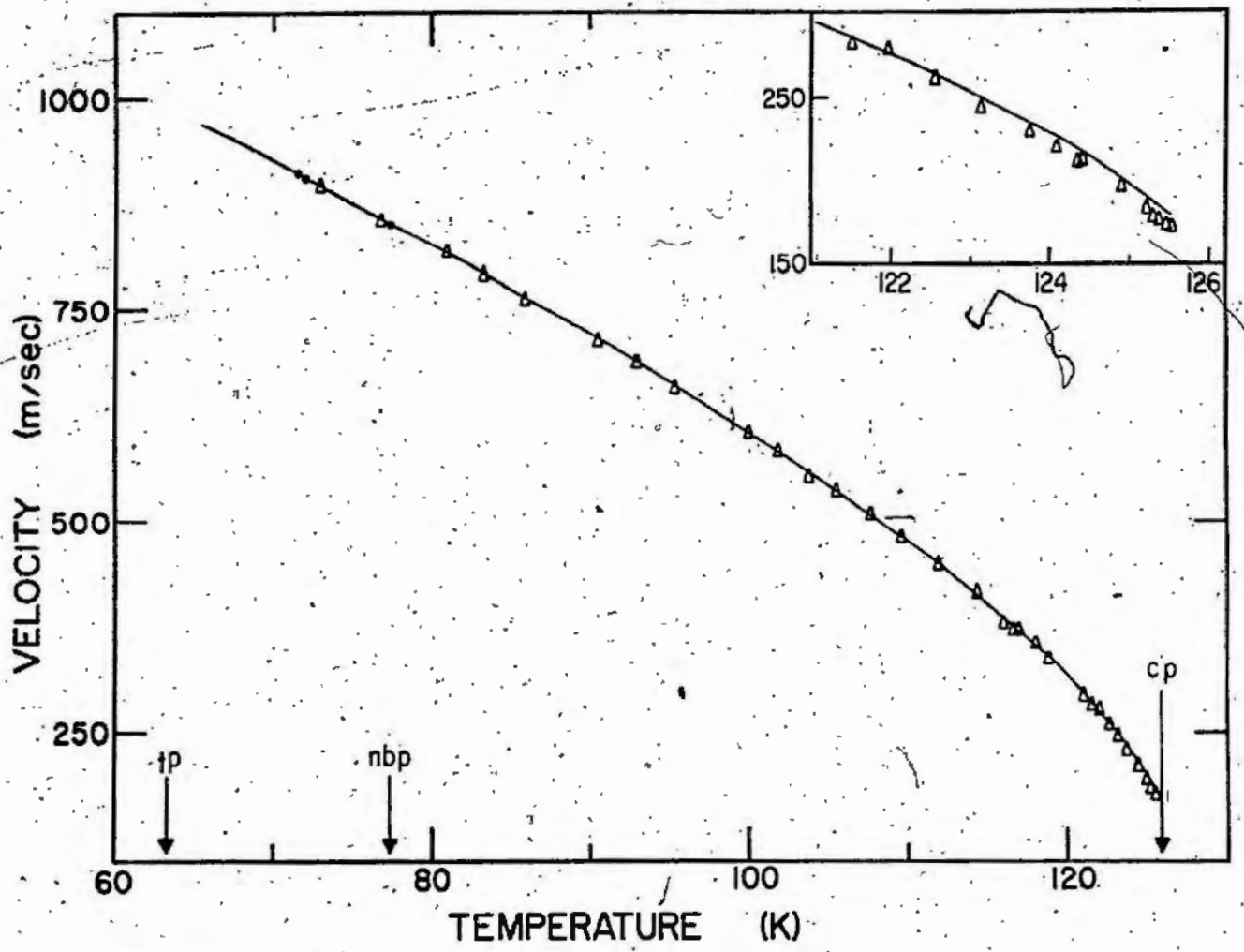
1000
750
500
250
VELOCITY (m/sec)
tp
nbp
cp
60
80
100
120
TEMPERATURE (K)
250
150
122
124
126

FIGURE 3.4

3.2 Error Analysis (Velocity)

From equation (3.1) we see that the accuracy of the velocity results obtained depends on the possible uncertainty in determining the following quantities:

(a) the frequency shift, $\Delta\nu$;

(b) the index of refraction, n;

(c) the scattering angle, θ;

(d) the wavelength, λ, of the laser light.

Each of these sources of error will be discussed in turn.

(a) Frequency shifts, $\Delta\nu$

The uncertainty in the measurement of the frequency shifts arises from two sources - instrumental errors affecting the location of the peaks as they were recorded and random errors associated with the actual measurement of the shifts.

Possible errors arising from fluctuations in the laser frequency were rendered negligible by the automatic frequency control described in Chapter 2, so that instrumental contributions to the error in $\Delta\nu$ were associated mainly with (i) non-linearities in the Fabry-Perot and other scanning electronics and (ii) line pulling effects which came into play at temperatures near the critical points where the Rayleigh and Brillouin lines began to overlap. This latter effect was only significant for a small number of the frequency shift measurements. The line pulling effects were estimated by graphical superposition, and the presence of this additional uncertainty will be indicated as appropriate in the data. The main instrumental contribution was, therefore, the

non-linearity in the voltage-versus-displacement function of the Fabry-Perot. This effect was systematic in nature and gave rise to a change in the separation of the adjacent Rayleigh peaks of about 1% between successive orders. The averaging procedures used in measuring the Brillouin shifts were found to reduce this error considerably and it will be treated in association with the random error determination to follow.

Since the interferometer was scanned through at least six orders for each temperature setting, the individual frequency shifts were measured for each order and then an average value was obtained as discussed previously (see Chapter 2). An examination of the scatter of the individual measurements about the mean value revealed that any systematic variations associated with the Fabry-Perot scanning mechanism were of the same order or less than the random measurement errors so that the standard or rms deviation of the individual frequency shifts from the average value was considered to be a reasonable estimate of the overall error in the frequency measurement, $\Delta\nu$. The percentage error thus obtained was obviously related to the magnitude of the frequency shift and therefore increased with temperature as the Brillouin shifts decreased.

The flat-plate separation of the Fabry-Perot was measured directly with a micrometer to an accuracy of better than 0.01% while the confocal plates were calibrated with respect to the flats to determine the free spectral range (see Chapter 2). Using this method, the estimated uncertainty (rms) in the value obtained for the FSR of the confocal plates was calculated to be $\sim$ 0.2%. In both cases, the

estimated error in the calculation of the FSR of the interferometer was negligible compared to the random errors in the measured frequency shifts.

The flat-plate interferometer was used throughout the temperature range investigated for both oxygen and nitrogen where it was found that the estimated (rms) errors in $\Delta\nu$ ranged from $\sim$ 0.3% at the lower temperatures to $\sim$ 1% near the critical points. However, the confocal plates were also used at the intermediate and higher temperatures of nitrogen where, due to its smaller FSR, the random error was found to $\sim$ 0.3% at T = 100 K to a maximum of $\sim$ 0.5% near the critical point.

(b) Index of refraction, n.

From the Lorentz-Lorenz relation used to calculate the index of refraction values, the accuracy of n depends on the accuracy of the density data, which was stated as $\sim$ 0.1%, and the assumed constancy of L. The values of n_o from Johns and Wilhelm (1937), used to calculate L were claimed accurate to at least 0.05% for both oxygen and nitrogen, while calculations showed that L varied by a maximum of only 0.2% for both liquids over the temperature ranges from 65 K to T_{nbp}.

The validity of the assumption of L being a constant for $T > T_{nbp}$ for oxygen was justified with reference to measurements of the static dielectric constant (ε) due to Younglove (1970). Using these values of ε and density data from Weber (1970) in the Clausius-Mossotti relation,

$$P = \frac{\varepsilon - 1}{\varepsilon + 2}\rho^{-1} \propto \frac{n^2 - 1}{n^2 + 2}\rho^{-1} \quad , \qquad (3.5)$$

the polarization, P, varied by a maximum of only 1% over the temperature range from T_{nbp} up to temperatures quite near the critical point. However, as pointed out by Younglove, this apparent density dependence of P was quite possibly due to inaccuracies in the measured densities especially at temperatures near the critical point. However, the value of n, calculated using equation (3.5), differed by a maximum of 0.2% from those calculated using a constant L and this value was expected to be a reasonable estimate of the error in the values of n used.

Unfortunately, there were no corresponding data available on liquid nitrogen to justify the assumed constancy of L directly in this case. However, based on the results obtained for liquid oxygen as well as similar results obtained for other liquids such as argon (Teague and Pings (1968)), this assumption was expected to hold equally well for nitrogen, also. In any case; the resulting error in n would be only 0.2% even if L varied by as much as 1.5% over the temperature range considered. Therefore, the uncertainty in n is estimated to be no greater than 0.2% even at the higher temperatures, while for the lower temperatures ($T \sim T_{nbp}$), the accuracy is probably better due to the smaller error in the value of L itself.

(c) Wavelength, λ

The wavelength, λ, of the incident laser beam was taken to be 514.5(4) nm and was assumed to be quite accurate since the laser frequency was stabilized by means of locking it to the side of the well-known iodine absorption line which is centered at 514.54 nm; therefore, assuming λ accurate to the fourth figure, i.e., λ = 514.5 nm, the resulting uncertainty would be only 0.08%. Laser 'jitter' and drift

of approximately 30 MHz (see Chapter 2) contributed an error of $\sim 10^{-5}$% to the absolute value of λ and was obviously quite negligible in comparison to the value quoted above.

(d). Scattering angle, θ

The scattering angle, θ, was determined by triangulation methods using a high quality pentaprism which is designed such that light incident on either surface is transmitted at exactly right angles to the incident path. The incident, Ar^+, laser beam was directed through the scattering cell as discussed previously while a second (He-Ne) laser was aligned such that its beam passed directly through the cell in coincidence with the axis of the collection optics. Possible refraction of the beams in passing through the optical windows in the cell and cryostat was minimized by taking care to ensure that the incident beams were normal to the respective windows; this was accomplished by careful alignment of the optics such that the incident and reflected beams coincided as closely as possible. The pentaprism was then placed into the path of the incident He-Ne beam, thereby redirecting it in the direction of the incident Ar^+ beam. The spatial separation between the two beams was first measured near the cell site and then as far as possible from the cell. Using elementary trigonometry, the difference between these two measurements was converted into an angular measurement. The resulting calculation showed θ to be 90.0° with a maximum uncertainty of 0.1%.

3.3 Overall Error in Velocity Determinations

By combining the individual uncertainties thus obtained, the resulting uncertainty in the velocity measurements were obtained. Equation (3.3) gives, for the velocity $\vec{V}$:

$$V = \frac{\lambda_i \nu_s}{2\, n\, \mathrm{Sin}\left(\frac{\theta}{2}\right)} \qquad (3.6)$$

By partial differentiation of equation (3.6), one obtains:

$$\frac{\Delta V}{V} = \frac{\Delta \lambda_i}{\lambda_i} + \frac{\Delta \nu_s}{\nu_s} - \frac{\mathrm{Cot}\left(\frac{\theta}{2}\right)}{2} \Delta\theta - \frac{\Delta n}{n} \qquad (3.7)$$

By substituting in the previously determined values of the uncertainty in λ_i, ν_s, n and θ, one finds that, to a good approximation, the estimated uncertainty in the velocity measurements ($\vec{V}$) arises primarily from the uncertainties in the frequency measurements ($\Delta\nu_i$), with combined contributions from the other sources being quite negligible in comparison to this major uncertainty. Therefore, it is felt that the estimated percentage uncertainty in the frequency shift measurements quite adequately represents the uncertainty in the velocity results.

3.4 Line Width Measurements and Attenuation

From Figures 3.1 and 3.2 we see that the Brillouin components tend to be noticeably broader than the central Rayleigh lines as well as tending to increase in width as the temperatures approach the critical points. This phenomenon is due to the damping of the sound waves which give rise to the Brillouin lines. According to classical arguments (see Chapter 1), this damping or attenuation is due to an

energy loss caused mainly by thermal conduction and viscous forces in the liquids.

Theory predicts (McIntyre and Sengers (1968)) that the true spectral lines very closely approximate Lorentzian line shapes; the central unshifted Rayleigh line, at the laser emission frequency, being highly Lorentzian with the full width at half-intensity maximum (FWHM), $\Delta\nu_R$, given by:

$$\Delta\nu_R = \frac{\kappa|\vec{K}|^2}{\pi C_p} \tag{3.8}$$

where $\vec{K}$ is the wave vector, κ is the thermal conductivity and C_p is the specific heat per unit volume. Because the ratio of the thermal conductivity to the specific heat is small in most liquids, $\Delta\nu_R$ is of the same order of magnitude as the laser line itself and requires much higher resolution than that obtained in this experiment to measure it accurately [for example, for oxygen at 86.1 K, $C_p \approx 0.468 \frac{cal}{cc\,^oK}$ and $\kappa \approx 3.64 \times 10^{-4} \frac{cal}{cm.s.\,^oK}$ (Victor and Beyer (1970))].

The damping or attenuation of the sound waves and the FWHM of the Brillouin lines are related by equation (1.32), thus:

$$\alpha(\vec{K}) = \frac{\pi\Delta\nu(\vec{K})}{V(\vec{K})} \tag{3.9}$$

where $\Delta\nu(\vec{K}) = \frac{\Gamma(\vec{K})}{\pi}$ is the FWHM of the Brillouin line;

$\alpha(\vec{K})$ is the amplitude absorption coefficient;

$V(\vec{K})$ is the sound velocity;

and $\Gamma(\vec{K})$ is the reciprocal lifetime of the sound wave.

Although the true Brillouin lines are closely Lorentzian, the actual recorded line shapes are affected by the detection system. The breadth of the recorded lines is affected by the finite width of the laser line, the detection by the interferometer as well as an aperture effect. This aperture effect is caused by the finite size of the limiting aperture, A_1 (see Figure 2.1), which admits light scattered through a small angle variation, thus contributing to a slight broadening of the Brillouin lines in accordance with equation (3.3). Therefore, an accurate determination of these line widths requires a careful convolution of the relevant line shapes, the accuracy of this method being ultimately limited by one's ability to determine these line shapes and measure the observed line widths accurately. In the present experiment and, on the basis of arguments presented below, the laser line was assumed to be a Gaussian shape while the interferometer's transmission function and the true Brillouin lines were assumed to be Lorentzian in shape.

The argon-ion laser used in this experiment was operated in the single-mode case and as such would be expected to result in a Lorentzian-type emission line. However, the relatively fast and random 'jitter' in the laser emission frequency was expected to cause the laser line to deviate from a Lorentzian in favour of a Gaussian (when sampling the line slowly, at least), which is more characteristic of the random events. This assumption was partially verified directly by observing the white card spectrum on an oscilloscope where most of the fast laser 'jitter' was resolved, thus showing the frequency fluctuations to be relatively large and quite random (to be discussed later).

To justify the assumed shape of the interferometer's transmission function, one can show that, for relatively high finesse, the general transmission function reduces to a Lorentzian. The Fabry-Perot transmission function is given generally by the Airy Formula (Stone (1963)):

$$T = \frac{T_{max}}{1 + F \sin^2 \varepsilon} \tag{3.10}$$

where T_{max} is the maximum transmission of the etalon;

F is the finesse of the instrument;

and ε is the relative phase difference between the interfering beams.

If we consider points near a transmission maximum, i.e., ε is close to $m\pi$ where m is an integer, then $\sin^2 \varepsilon = \sin^2 (\varepsilon - m\pi) \approx (\varepsilon - m\pi)^2$. Then equation (3.10) reduces to:

$$T \approx \frac{T_{max}}{1 + F \sin^2 \varepsilon} \approx \frac{T_{max}}{1 + F(\varepsilon - m\pi)^2} = \frac{T_{max} \frac{1}{F}}{\frac{1}{F} + (\varepsilon - m\pi)^2} \tag{3.11}$$

which is a Lorentzian line shape valid for small ε. For $F = 120$, $\varepsilon \approx 1/F \approx \sin \varepsilon$ to the seventh decimal place; this approximation holds with good accuracy for $F \geq 30$.

The assumed shape of the Brillouin lines is based on present theory (see Chapter 1) which suggests that these lines are highly Lorentzian in shape.

In the special case that all the relevant line shapes are Lorentzian, the deconvolution procedure is greatly simplified since the individual line widths then add directly to give the total observed FWHM

of the Brillouin lines, with the true FWHM, $\Delta\nu_B'$, being obtained via the following equation:

$$\Delta\nu_B' = (\Delta\nu_{obs} - \Delta\nu_I) \tag{3.12}$$

where $\Delta\nu_{obs}$ is the observed FWHM of the Brillouin lines and $\Delta\nu_I$ is the FWHM of the instrumental line (laser line modified by detection with the interferometer). However, the case of a convolution of one Gaussian and two Lorentzian line shapes requires a more detailed analysis.

The deconvolution procedure used to analyze the Brillouin lines was based on the results of a study by Leidecker and LaMacchia (1968) who performed the convolution of the Gaussian and Lorentzian functions and determined the necessary formulae and tables of data needed to correct the observed spectral line widths. The resulting equations thus obtained were:

$$\Delta\nu_B' = \Delta\nu_{obs} - F[(\Delta\nu_{obs}/\Delta\nu_L)|a_I]\ \Delta\nu_I \tag{3.13}$$

and

$$a_I = (\ell n 2)^{\frac{1}{2}}\ \Delta\nu_{FP}/\Delta\nu_I \tag{3.14}$$

where $\Delta\nu_B'$, $\Delta\nu_I$ and $\Delta\nu_{obs}$ are the same as in equation (3.12);

a_I is a parameter which measures the characteristic shape of the instrumental line;

$\Delta\nu_{FP}$ and $\Delta\nu_L$ are the FWHM's of the Fabry-Perot and laser lines, respectively;

and $F[(\Delta\nu_{obs}/\Delta\nu_L)|a_I]$ is a correction factor from the special case of all Lorentzian lineshapes.

The function F was evaluated by Leidecker and LaMacchia (1968) and given in tabular form. Therefore, to perform these corrections, it was necessary to determine $\Delta\nu_L$, $\Delta\nu_{FP}$ and $\Delta\nu_I$ from the experimental setup.

The instrumental line was obtained by recording the spectrum of the laser light scattered from a white card placed in front of the interferometer as discussed in Chapter 2. These spectra were taken immediately before and after the Brillouin spectra were recorded to check against possible misalignment during the process. They were then analyzed in the usual manner described earlier and the FWHM, $\Delta\nu_I$, obtained.

The determination of $\Delta\nu_{FP}$ and $\Delta\nu_L$ was a more difficult problem since both these contributions were of the same order of magnitude and could not be experimentally isolated from each other in any straightforward manner. For example, the most direct method of determining $\Delta\nu_{FP}$ would be to record the spectrum (scattered from a white card) of a source whose frequency bandwidth was small compared to $\Delta\nu_{FP}$, with the latter condition being, in principle, established by observing that the instrumental width $\Delta\nu_I$ is not affected by a further decrease in source bandwidth. However, the achievement of a source width less than the $\Delta\nu_L$ used in the present experiment is extremely difficult, and such a source was certainly not available. Similar comments also apply to the possible determination of $\Delta\nu_L$ by employing an interferometer whose bandpass is small compared to $\Delta\nu_L$; the achievement of a stable interferometer transmission function whose width is very much less than that provided by the present (confocal) instrument is likewise extremely

difficult. In short, the limitations imposed in this connection are those of the current state of the art in laser and interferometer technology.

Fortunately, however, it was possible to utilize the fast-scanning capability of the present interferometer to arrive at estimates of $\Delta\nu_{FP}$ and $\Delta\nu_L$. The procedure was to examine the instrumental width $\Delta\nu_I$ in the manner described above but, instead of using a strip chart recorder, the spectrum was displayed on an oscilloscope screen with much shorter sweep times. By decreasing the sweep periods of the interferometer and oscilloscope in synchronism, it was found that the instrumental line underwent a change from being stable but relatively broad to being considerably narrower but erratic in its behaviour. This latter situation corresponded to sweep periods of $\sim$ 100 ms or less and it was apparent that the random and abrupt changes in the laser frequency were being (at least partially) resolved in time. The minimum instrumental width observed under these conditions, i.e., $\sim$ 6.5 MHz, was taken to correspond to $\Delta\nu_{FP}$ and this choice can be justified by noting that it corresponds to a finesse of $\sim$ 150 which can quite reasonably be expected for a good spherical Fabry-Perot. In addition, the rms deviation of this 6.5 MHz line from its mean position on the oscilloscope screen was found to correspond approximately to 15 MHz, and this was taken as an estimate of the width, $\Delta\nu_L$, which would be observed during the much longer sweep periods characteristic of the normal recording process.

These experimentally determined values of $\Delta\nu_L$, $\Delta\nu_{FP}$ and $\Delta\nu_I$ were then used in conjunction with equations (3.13) and (3.14) as well as the tabulated data of Leidecker and LaMacchia (1968) to determine the

necessary corrections to the observed line widths, $\Delta\nu_{obs}$, thus obtaining the corrected FWHM, $\Delta\nu_B'$, of the Brillouin lines.

A further correction was now necessary to account for the aperture effect mentioned previously. To determine this effect of the angular size of the limiting aperture, A_1, we obtain from equation (3.3) upon differentiating with respect to θ:

$$\frac{\partial \nu_s}{\partial \theta} = \frac{nV}{\lambda_i} \text{Cos} \left(\frac{\theta}{2}\right) \quad . \tag{3.15}$$

Thus:

$$\Delta\nu_A \simeq \frac{nV}{\lambda_i} \text{Cos} \left(\frac{\theta}{2}\right) \Delta\theta = \nu_s \text{Cot} \left(\frac{\theta}{2}\right) \frac{\Delta\theta}{2} \tag{3.16}^*$$

where $\Delta\nu_A$ is the aperture broadening contribution and $\Delta\theta$ is the angle subtended by the aperture at the scattering site, which was calculated to be $\simeq 0.011$ radians in the present experiment.

The corresponding value of $\Delta\nu_A$ was then subtracted directly from the corrected value, $\Delta\nu_B'$, to obtain the value, $\Delta\nu_B$, the FWHM of the Brillouin line. Tables 3.3 and 3.5 show the results obtained for $\Delta\nu_B$ along with the relevant data used to obtain the necessary corrections to $\Delta\nu_{obs}$ for both N_2 and O_2, respectively. Using the values of $\Delta\nu_B$ thus obtained, the amplitude absorption coefficient, $\alpha(\vec{K})$, was then calculated using equation (3.9); that is,

$$\alpha(\vec{K}) = \frac{\pi \Delta\nu_B(\vec{K})}{V(\vec{K})} \quad . \tag{3.17}$$

The experimental data thus obtained for $\Delta\nu_B$ and α are presented in Tables 3.4 and 3.6 for liquid N_2 and O_2, respectively, while

---

*From here on, ν_s will be written as ν for convenience.

TABLE 3.3

Brillouin line width data for saturated liquid nitrogen*

T(K)	ν (GHz)	$\Delta\nu_{obs}$ (MHz)	$\Delta\nu_I$ (MHz)	F ←	$\Delta\nu_B'$ (MHz)	$\Delta\nu_A$ (MHz)	$\Delta\nu_B$ (MHz)
91.3(7)	2.287	40.5	17.1	0.633	29.7	12.4	17.3
95.2(5)	2.136	40.0	17.1	0.637	29.1	11.6	17.5
101.7(9)	1.870	38.9	17.1	0.645	27.8	10.1	17.7
105.0(3)	1.726	42.0	16.4	0.611	32.0	9.34	22.7
107.5(4)	1.616	42.7	16.4	0.607	32.7	8.75	24.0
108.6(8)	1.562	41.7	16.4	0.613	31.6	8.45	23.2
113.5(5)	1.390	42.2	16.4	0.610	32.1	7.52	24.6
114.4(5)	1.287	41.7	16.4	0.613	31.6	6.96	24.6
115.7(0)	1.219	43.2	16.4	0.604	33.3	6.60	26.7
116.9(8)	1.147	41.1	16.4	0.617	31.0	6.20	24.8
118.0(1)	1.115	43.6	16.4	0.602	33.7	6.03	27.7
122.5(8)	0.8097	54.5	16.4	0.551	45.4	4.38	41.0
123.1(4)	0.7575	64.1	16.4	0.522	55.5	4.10	51.4
124.1(0)	0.6777	66.4	16.4	0.517	57.9	3.67	54.2
124.4(2)	0.6495	70.7	16.4	0.508	62.4	3.52	58.9
124.9(0)	0.6022	79.2	16.4	0.490	71.1	3.25	67.9

*For a discussion of errors, see page 86.

TABLE 3.4

Hypersonic absorption coefficient data for saturated liquid nitrogen*

T(K)	V (ms^{-1})	ν (GHz)	$\Delta\nu_B$ (MHz)	$\alpha = \frac{\pi\Delta\nu_B}{V}$ (cm^{-1})	$\frac{\alpha}{\nu^2} \times 10^{16}$ ($cm^{-1}s^2$)
91.3(7)	704.2	2.287	17.3	771	1.48
95.2(5)	660.8	2.136	17.5	833	1.83
101.7(9)	583.2	1.870	17.7	954	2.73
150.0(3)	540.9	1.726	22.7	1320	4.42
107.5(4)	508.4	1.616	24.0	1480	5.67
108.6(8)	492.2	1.562	23.2	1480	6.06
113.5(5)	441.8	1.390	24.6	1750	9.06
114.4(5)	409.8	1.287	24.6	1890	11.4
115.7(0)	389.4	1.219	26.7	2160	14.5
116.9(8)	367.3	1.147	24.8	2120	16.1
118.0(1)	357.8	1.115	27.7	2430	19.6
122.5(8)	263.5	0.8097	41.0	4890	74.6
123.1(4)	247.0	0.7575	51.4	6540	114
124.1(0)	221.0	0.6777	54.2	7710	168
124.4(2)	213.1	0.6495	58.9	8680	206
124.9(0)	198.0	0.6022	67.9	10,800	297

*For a discussion of errors, see page 86.

TABLE 3.5

Brillouin line width data for saturated liquid oxygen*

T(K)	ν (GHz)	$\Delta\nu_{obs}$ (MHz)	F	$\Delta\nu_B'$ (MHz)	$\Delta\nu_A$ (MHz)	$\Delta\nu_B$ (MHz)
98.7(2)	2.801	42.9	0.665	30.1	15.2	15.0
105.0(5)	2.602	42.4	0.660	29.5	14.1	15.4
115.8(1)	2.250	43.1	0.654	30.3	12.2	18.1
126.5(6)	1.856	36.4	0.711	22.5	10.0	12.5
134.8(6)	1.552	38.4	0.692	24.9	8.40	16.5
143.0(7)	1.202	40.6	0.674	27.4	6.50	20.9
149.8(8)	0.8428	50.1	0.611	38.1	4.56	33.6
152.3(5)	0.6816	71.1	0.534	60.6	3.69	56.9
153.7(5)	0.5456	81.3	0.513	71.3	2.95	68.4

*For a discussion of errors, see page 86.

TABLE 3.6

Hypersonic absorption coefficient data for saturated liquid oxygen*

T(K)	V (ms^{-1})	ν (GHz)	$\Delta\nu_B$ (MHz)	$\alpha = \frac{\pi\Delta\nu_B}{V}$ (cm^{-1})	$\frac{\alpha}{\nu^2} \times 10^{16}$ ($cm^{-1}s^2$)
98.7(2)	838.0	2.801	15.0	561	0.715
105.0(5)	782.8	2.602	15.4	617	0.912
115.8(1)	684.3	2.250	18.1	831	1.64
126.5(6)	571.6	1.856	12.5	685	1.99
134.8(6)	483.5	1.552	16.5	1070	4.45
143.0(7)	379.9	1.202	20.9	1730	12.0
149.8(8)	271.2	0.8428	33.6	3890	54.8
152.1(5)	221.5	0.6816	56.9	8080	174
153.7(5)	179.1	0.5456	68.4	12,000	403

*For discussion of errors, see page 86.

corresponding plots of $\frac{\alpha}{\nu^2}$ vs. T and ν as well as α vs. T and ν are presented in Figures 3.5 through 3.8.

3.5 Error Analysis (Line Width)

The estimated uncertainty in the values obtained for $\Delta\nu_B$ arose from two main sources: the accuracy with which $\Delta\nu_{obs}$ could be measured from the recorded spectra and the validity of the assumptions made in the deconvolution procedure.

An rms fit of the individually measured values of $\Delta\nu_{obs}$ was made for each recorded spectrum and it was found that the uncertainty in the mean value of $\Delta\nu_{obs}$ ranged from a maximum of $\sim$ 7% for the narrowest lines (i.e., lowest temperatures) to less than $\sim$ 5% at the higher values. This uncertainty was due mainly to the low S/N ratio for the Brillouin lines which, because they were so relatively narrow, introduced significant error in the measurement of any individual line width.

The main sources of error in the deconvolution procedure were expected to arise due to the assumption made concerning the relevant line shapes as well as from the determination of $\Delta\nu_L$ and $\Delta\nu_{FP}$. However, calculations showed that the corrections made were relatively insensitive to the values of $\Delta\nu_{FP}$ and $\Delta\nu_L$ used with an error of $\sim$ 20% in the value of a_I, causing a corresponding error of a maximum of $\sim$ 3.5% in the lowest value of $\Delta\nu_B$ obtained, while for the higher values, the resulting error was only $\sim$ 1%. Although it was difficult to determine the total possible uncertainty due to the line shape assumptions, it was expected that a reasonable estimate of the total

FIGURE 3.5

Plot of the absorption coefficient (α) divided by the square of the hypersonic frequency (ν^2), as a function of temperature (T) and frequency (ν) for saturated liquid oxygen. (nbp - normal boiling point; cp - critical point.). The solid curve represents a 'best fit' to the present data points (open circles). For the higher temperatures (i.e., $|T - T_c| \leq 10$ K), the results are estimated to be accurate to at least ± 15% while, for the lower temperatures, the uncertainty may be greater.

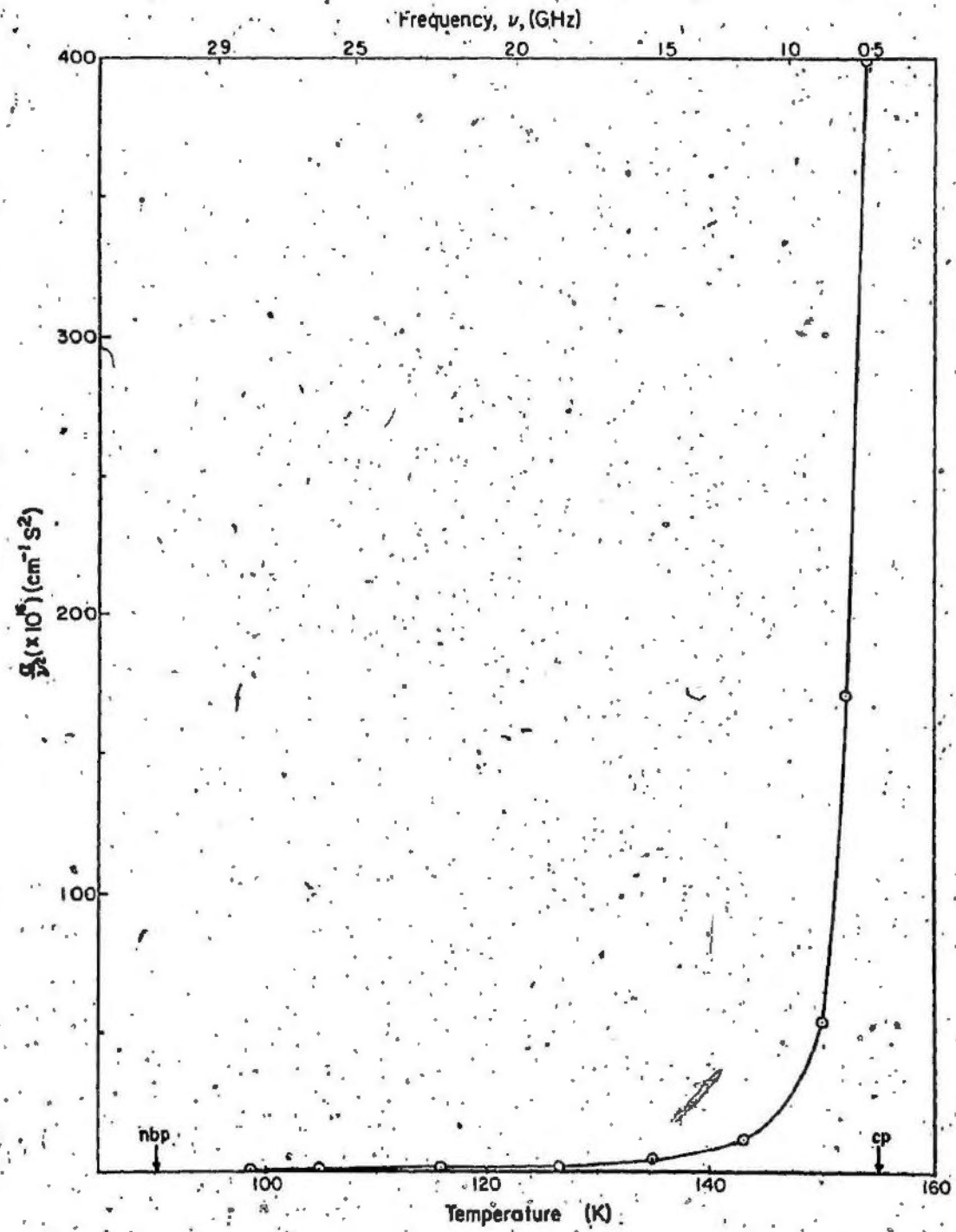
Frequency, ν, (GHz)
29
25
20
15
10
05
400
300
200
100
$\frac{S_{\Delta\nu}}{\nu^2}(\times 10^{15})(cm^{-1}s^2)$
nbp
cp
100
120
140
160
Temperature (K)

FIGURE 3.5

FIGURE 3.6

Plot of the absorption coefficient (α) divided by the square of the hypersonic frequency (ν^2), as a function of temperature (T) and frequency (ν) for saturated liquid nitrogen. (nbp - normal boiling point; cp - critical point.) The solid curve represents a 'best fit' to the present data points (open circles). For the higher temperatures (i.e., $|T - T_c| \leq 10$ K) the results are estimated to be accurate to at least ± 15% while, for the lower temperatures, the uncertainty may be greater. The triangles represent the data points of Pine (1969) to a claimed accuracy of ± 10%.

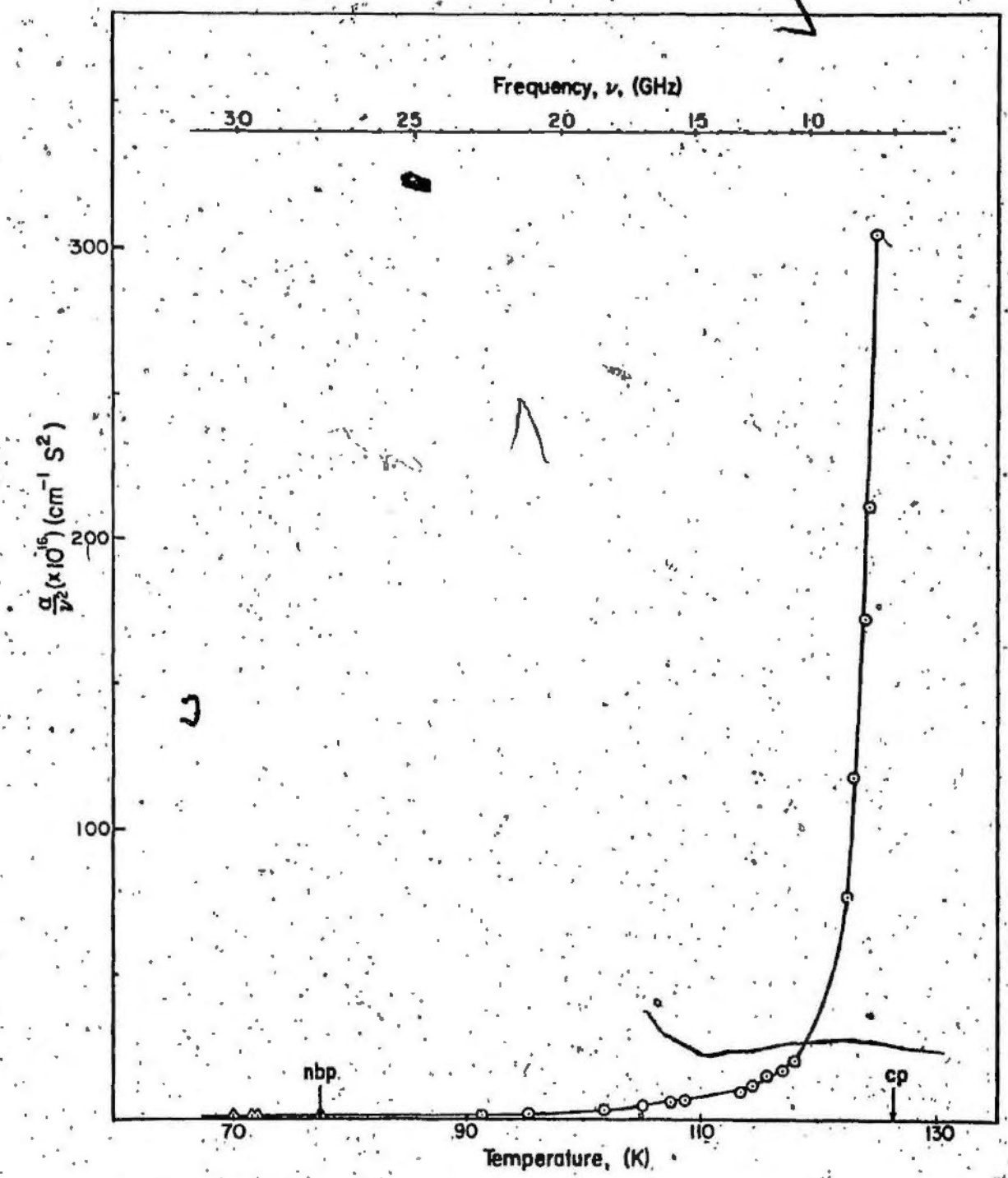
Frequency, ν, (GHz)
30
25
20
15
10
300
200
100
$\frac{\alpha}{\nu^2}(\times 10^{16})\ (cm^{-1}\ S^2)$
nbp
cp
70
90
110
130
Temperature, (K)

FIGURE 3.6

FIGURE 3.7

Plot of the absorption coefficient (α) vs. temperature (T) and frequency (ν) for saturated liquid oxygen. (nbp - normal boiling point; cp - critical point.) The solid curve represents a 'best fit' to the present data points (open circles). (For $|T - T_c| \leq 10$ K, the data are expected to be accurate to at least ± 15% while, for the lower temperatures, greater uncertainty may exist.)

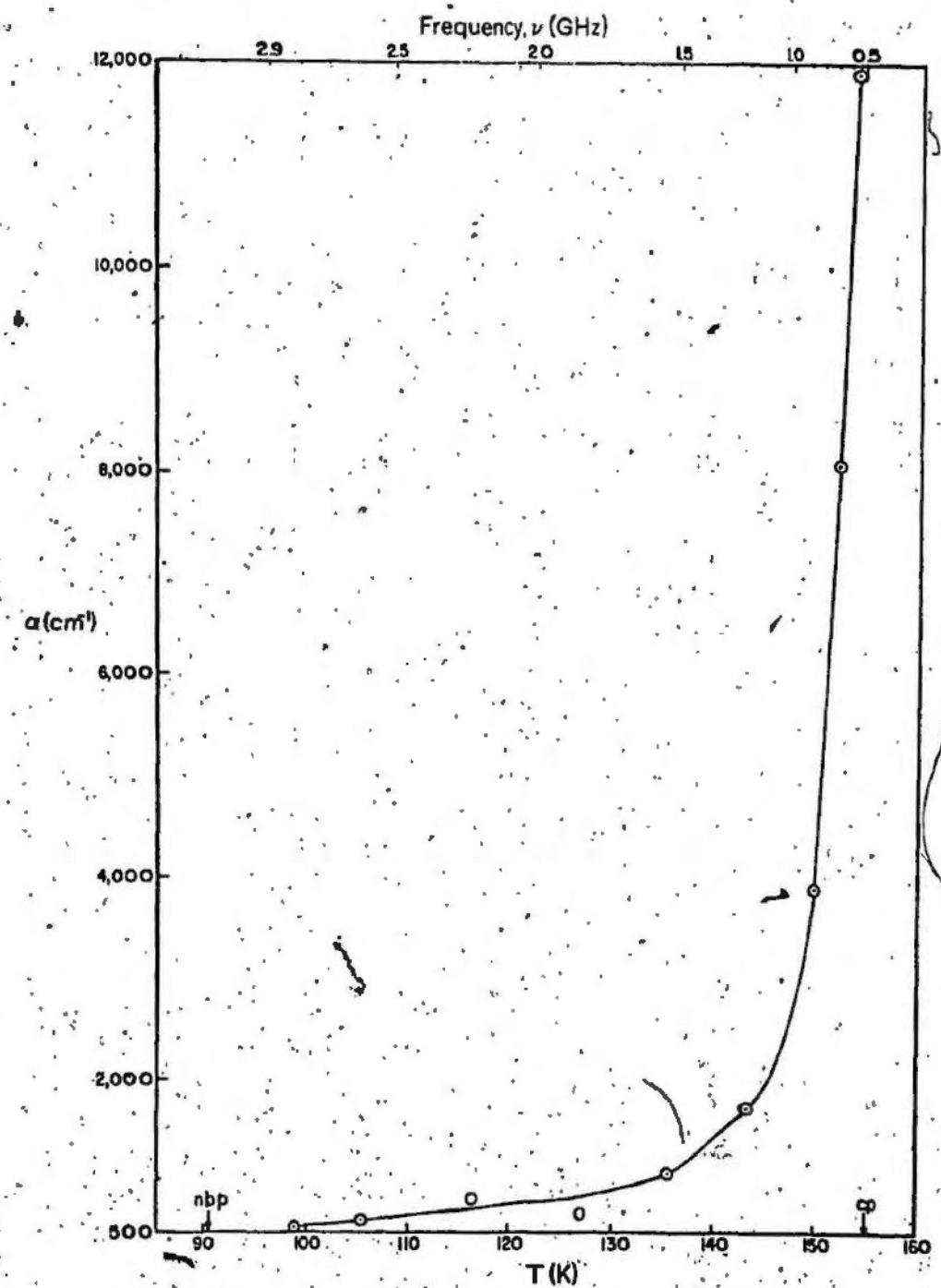
Frequency, ν (GHz)
2.9
2.5
2.0
1.5
1.0
0.5
12,000
10,000
8,000
6,000
4,000
2,000
500
α(cm⁻¹)
nbp
90
100
110
120
130
140
150
160
T(K)

FIGURE 3.7

FIGURE 3.8

Plot of the absorption coefficient (α) vs. temperature (T) and frequency (ν) for saturated liquid nitrogen. (c_p - critical point.) The solid curve represents a 'best fit' to the present data points (open circles). (For $|T - T_c| \leq 10$ K, the data are expected to be accurate to at least $\pm$ 15% while, for the lower temperatures, greater uncertainty may exist.)

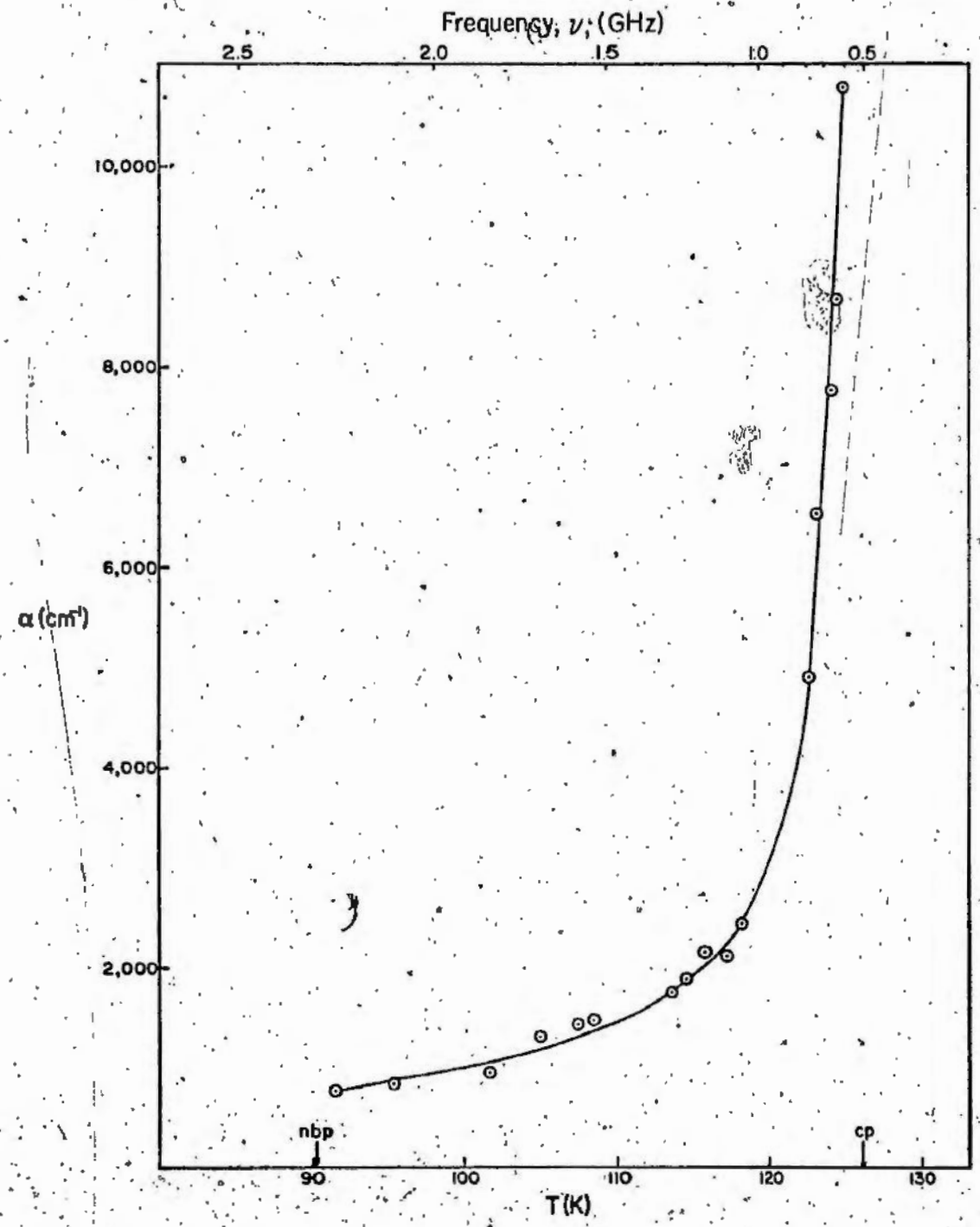
Frequency, ν, (GHz)
2.5
2.0
1.5
1.0
0.5
10,000
8,000
6,000
4,000
2,000
α (cm⁻¹)
nbp
cp
90
100
110
120
130
T(K)

FIGURE 3.8

uncertainty arising from the deconvolution procedure should be in the neighbourhood of 5% to 10%. At the lower temperatures, however, knowledge of the exact aperture (A_1 in Figure 2.1) size is extremely critical since the aperture correction is of the same order of magnitude as the estimated Brillouin line widths (see Tables 3.3 and 3.5). The error in this correction at the lower temperatures could be as large as $\sim$ 50% due to the uncertainty in the measurement of the aperture (A_1) radius. However, the results at the higher temperatures which are specifically of interest in this research are estimated to be accurate to $\pm$ 15%.

CHAPTER 4

DISCUSSION OF RESULTS

4.1 Velocity

As shown in the tabulated data of Tables 3.1 and 3.2 as well as the plotted graphs of velocity versus temperature in Figures 3.3 and 3.4, there is good agreement, for both liquid O_2 and N_2, between the hypersonic velocities obtained in the present experiments and the corresponding ultrasonic data obtained from the literature, except for temperatures within a few degrees of the respective critical points. In this region there appears to be a significant negative dispersion in the sound velocity; that is, the hypersonic velocities become progressively lower than the ultrasonic velocities as the critical point is neared for both liquids. The most marked difference between the two occurs for liquid oxygen where the discrepancy ranges from ≈ 4% at 150 K to ≈ 13% at 153.9 K (T_c = 154.58 K), well above the estimated experimental error of a maximum of ∿ 1% (see Error Analysis, Chapter 3) in this region. For the case of nitrogen, however, this effect is not as great with the observed discrepancy ranging from ≈ 1% at 123.74 K to ≈ 3% at 125.52 K (T_c = 126.26 K) with the estimated uncertainty in the experimental results again ∿ 1%.

These curves show behaviour similar to results obtained in other liquids such as xenon (Chase et al. (1964); Mueller et al. (1972)) and HCl (Greazeale (1962)), with the observed dispersion occurring in the critical region as expected from theoretical considerations. Although

the present results are not conclusive due to an inability to study the critical temperatures more closely, the observed velocities decrease so sharply as the critical temperatures are approached that a zero value of the velocity at the critical point (as predicted by theory) does not appear unreasonable.

Although, to our knowledge, there have been no similar Brillouin studies completed on these liquids with which to compare the results obtained in this region, it is felt that this dispersion represents a real physical effect.

4.2 Line Width

Figures 3.5 to 3.8 show the behaviour of the absorption coefficient, α, of liquid O_2 and N_2 with respect to temperature and frequency. These curves clearly indicate the anomalous behaviour of the absorption coefficient near the critical point as predicted by theory (see Chapter 1). Similar behaviour has been observed in other liquids (Fixman (1962); Ford et al. (1968); Mueller et al. (1972)) although few Brillouin scattering results have been reported on oxygen or nitrogen; in fact, with the exception of Pine (1969) who measured α for a few temperatures below the normal boiling point in liquid nitrogen, no other Brillouin scattering results could be found in current literature, especially for the higher temperature regions of these liquids which were of particular interest in this research.

For temperatures sufficiently removed from the critical regions, Figures 3.5 and 3.6 show that $\frac{\alpha}{\nu^2}$ varies approximately linearly with

temperature. When extrapolated towards the triple point, the present results appear to agree reasonably well with the limited results of Pine (1969) despite the fact that considerable uncertainty may exist in our lower temperature values of α in this region (see Error Analysis, Chapter 3).

However, as we move towards the critical point, T_c, the attenuation coefficient is seen to increase relatively slowly at first up to $|T-T_c| \simeq 10$K (see Figures 3.3 and 3.5); then the slope of the curves increases dramatically thereafter. This general behaviour was also reflected in the recorded spectra where a correspondingly dramatic increase in the widths of the Brillouin lines was also observed. As mentioned previously, such a behaviour appears to be characteristic of this critical region.

Due to a lack of sufficiently accurate values of the thermodynamic quantities (λ, γ, κ, C_v and η_{sh}) arising in the absorption coefficient equation (1.49), no attempts were made to plot the classical contributions, α_{cl}, to the absorption coefficient in order to evaluate α'. However, for the lower temperatures, where the critical relaxational phenomena are absent, the main contribution to α is expected to be α_{cl}.

BIBLIOGRAPHY

Benedek, G. and Greytak, T., Proc. IEEE, 53, 1623 (1965).

Benedek, G., Lastovka, J. B., Fritsch, K. and Greytak, T., J. Opt. Soc. Am., 54, 1284 (1964).

Bhatia, A. B., Ultrasonic Absorption (Oxford University Press, 1967).

Breazeale, M. A., J. Chem. Phys., 36, 2530 (1962).

Brillouin, L., Compt. Rend., 158, 1331 (1914).

Brillouin, L., Ann. Phys. (Paris), 17, 88 (1922).

Cannell, D. S. and Benedek, G. B., Phys. Rev. Letters, 25, 1157 (1970).

Chase, C. E., Williamson, R. C. and Tesza, L., Phys. Rev. Letters, 13, 467 (1964).

Chiao, R. Y. and Stoicheff, B. P., J. Opt. Soc. Am., 54, 1286 (1964).

Chynoweth, A. G. and Schneider, W. G., J. Chem. Phys., 20, 1777 (1952).

Clouter, M. J., Kiefte, H. and Morgan, I.E., Can. J. Phys., 53 1727 (1975).

D'Arrigo, G. and Sette, D., J. Chem. Phys., 48, 691 (1968).

Eden, D., Garland, C. W. and Thoen, J., Phys. Rev. Letters, 28, 726 (1972).

Fabelinskii, I. L., Molecular Scattering of Light (Plenum Press, New York, 1968).

Fixman, M., J. Chem. Phys., 36, 1961 (1962).

Ford, N. C., Langley, K. H. and Puglielli, V. G., Phys. Rev. Letters, 20, 9 (1968).

Gornal, W. S., M.Sc. Thesis, University of Toronto (1966).

Gross, E., Nature, 126, 201, 400, 603 (1930).

Gross, E., Nature, 129, 722 (1932).

Herzfeld, K. F. and Litovitz, T. A., Absorption and Dispersion of Ultrasonic Waves (Academic Press, New York (1959)).

Hohimer, J. P., Kelly, R. C. and Tittel, F. K., Appl. Opt., 11, 626 (1972).

Johns, H. E. and Wilhelm, J. O., Can. J. Res., 15, 101 (1937).

Krishnan, R. S., Proc. Indian Acad. Sci., A41, 91 (1955).

Leidecker, H. W. and LaMacchia, J. T., J. Acoust. Soc. Am., 43, 143 (1968).

Matheson, A. J., Molecular Acoustics (Wiley-Interscience, London, 1970), p. 9.

McIntyre, D. and Sengers, J. V., Physics of Simple Liquids, edited by Temperley, H. N. V., Rowlinson, J. S. and Rushbrook, G. S. (Wiley-Interscience, New York, 1968), p. 447.

Mohr, R., Langley, K. H. and Ford, N. C., Jr., J. Acoust. Soc. Am., 49, 1030 (1971).

Mueller, P. E., Eden, O., Garland, C. W. and Williamson, R. C., Phys. Rev., A6, 2272 (1972).

Pine, A. S., J. Chem. Phys., 51, 5171 (1969).

Roder, H. M., McCarty, R. D. and Johnson, V. J., NBS Technical Note #361 (1968).

Sette, D., Physics of Simple Liquids, edited by Temperley, H. N. V., Rowlinson, J. S. and Rushbrook, G. S. (Wiley-Interscience, New York, 1968), p. 325.

Stanley, H. E., Introduction to Phase Transitions and Critical Phenomena (Oxford University Press, New York, 1971), p. 233ff.

Stone, J. M., Radiation and Optics (McGraw-Hill, New York, 1963), p. 406ff.

Teague, R. K. and Pings, C. J., J. Chem. Phys., 48, 4973 (1968).

Van Dael, W., Van Itterbeek, A., Cops, A. and Thoen, J., Physica, 32, 611 (1966).

Venkateswaren, C. S., Proc. Indian Acad. Sci., A15, 322, 362 (1942).

Victor, A. E. and Beyer, R. T., J. Chem. Phys., 52, 1573 (1970).

Weber, L. A., J. Res. Nat. Bur. Stand., A74, 93 (1970).

Weber, L. A., Advances in Cryogenic Engineering, vol. 15 (Plenum Press, New York, 1970); p. 50.

Wong, L. Y. and Anderson, A., J. Opt. Soc. Am., 62, 112 (1972).

Younglove, B. A., Advances in Cryogenic Engineering, vol. 15 (Plenum Press, New York, 1970), p. 70.